Europe
European Chemical
Societies Publishing

Special Collection

Assessing the Reactivity of Hard Carbon Anodes: Linking Material Properties with Electrochemical Response Upon Sodium- and Lithium-Ion Storage

Hyein Moon,[a, b] Maider Zarrabeitia,[a, b] Erik Frank,[c] Olaf Böse,[a, b, d] Marina Entería,[e] Damien Saurel,[e] Ivana Hasa,*[a, b, f] and Stefano Passerini*[a, b]

Hard carbon (HC) is the negative electrode (anode) material of choice for sodium-ion batteries (SIBs). Despite its advantages in terms of cost and sustainability, a comprehensive understanding of its microstructure is not complete yet, thus hindering a rational design of high-performance HC electrodes. In this study, rather than investigating how the precursor and synthesis method influence on the electrochemical properties of HC anodes, we examine the microstructure and surface chemistry of three optimized HC anodes obtained from different precursors by using different synthesis routes. The main goal is to evaluate the influence of the final materials properties (in their optimized state) on the electrochemical reactivity in lithium and sodium cells after a comprehensive structural characterization performed by means of X-ray photoelectron spectroscopy (XPS), wide-angle X-ray scattering (WAXS), Raman spectroscopy, scanning electron microscopy (SEM), and gas sorption measurements. The different electrochemical performance observed in terms of cycling stability and rate capability, and the stability of the solid electrolyte interphase (SEI) formed on the various HCs have been comprehensively investigated. A correlation of the material properties with their electrochemical response upon sodium and lithium uptake and release is clarified. By comparing the Na- and Li-ion storage behavior, a structure-function relation is identified.

1. Introduction

Sodium-ion batteries (SIBs) are considered one of the most promising next-generation energy storage devices. Owing to their potentially lower cost and higher sustainability compared to the current lithium-based technology, SIBs have the potential to share the future stationary storage market as well as become a dominant technology for high power automotive applications and light electric vehicles.[1–4] Indeed, several cell prototypes have been proposed demonstrating the real potential of sodium-based technology. Among them, the first 18650 cylindrical SIB cell using hard carbon (HC) as anode and $Na_3V_2(PO_4)_2F_3$ (NVPF) as the cathode has been jointly proposed by the French National Centre for Scientific Research (CNRS) and the French Alternative Energies and Atomic Energy Commission (CEA).[5] Alternative cell chemistries employing layered oxide and Prussian blue cathodes have been proposed by Faradion in UK,[6] Hi–Na battery in China,[7] Natron Energy Inc.,[8] Sharp Laboratories of America Inc. and Novasis Energies Inc. in the United States.[9]

Interestingly, while the cathode electrode chemistry is very diverse, HC represents the anode of choice for all the proposed sodium cell prototypes (except for Natron and Hi–Na) confirming the dominant position of HC among other types of anode materials.

In the 80's, HC was also considered a promising anode material for application in LIBs. Indeed, the second generation of lithium-ion cells included a HC anode and exhibited a 10% increase in volumetric energy density compared to the first generation (using a polyacetylene based anode) and was rated at ~130 Wh Kg^{-1}.[10,11] Despite the remarkable improvement,[12–16] HC anode implementation resulted in a huge first cycle irreversible capacity, which consumed significant amounts of Li from the cathode and required extra cathode capacity to compensate, lowering the overall energy density.[11] In addition, the flat voltage plateau of graphite was

---

[a] H. Moon, Dr. M. Zarrabeitia, Dr. O. Böse, Dr. I. Hasa, Prof. S. Passerini
Helmholtz Institute Ulm (HIU)
Helmholtzstrasse 11, 89081 Ulm, Germany
E-mail: ivana.hasa@warwick.ac.uk
stefano.passerini@kit.edu
[b] H. Moon, Dr. M. Zarrabeitia, Dr. O. Böse, Dr. I. Hasa, Prof. S. Passerini
Karlsruhe Institute of Technology (KIT)
P.O. Box 3640, 76021 Karlsruhe, Germany
[c] Dr. E. Frank
Deutsche Institute für Textil- und Faserforschung Denkendorf (DITF)
Körschtalstr. 26, 73770 Denkendorf, Germany
[d] Dr. O. Böse
Zentrum für Sonnenenergie-und Wasserstoff-Forschung Baden-Württemberg (ZSW)
Lise-Meitner-Str. 24, 89081 Ulm, Germany
[e] Dr. M. Entería, Dr. D. Saurel
Centre for Cooperative Research on Alternative Energies (CIC energiGUNE)
Basque Research and Technology Alliance (BRTA)
Alava Technology Park, Albert Einstein 48, 01510 Vitoria-Gasteiz, Spain
[f] Dr. I. Hasa
WMG, The University of Warwick
Coventry CV4 7AL, United Kingdom

Supporting information for this article is available on the WWW under https://doi.org/10.1002/batt.202000322

An invited contribution to a joint Special Collection between ChemElectroChem and Batteries & Supercaps dedicated to research Beyond Lithium-Ion Batteries

highly desired compared to the sloppy voltage profile of HC, thus when graphite could be efficiently employed in polypropylene carbonate free electrolytes, the use of HC anodes was dismissed.[11]

On the other hand, graphite cannot be used in carbonate-based sodium-ion cells so the predominant anode of choice is still hard carbon. Despite the promising properties, several disadvantages affect the performance of HC as anode material, such as the poor initial coulombic efficiency (ICE), the low power performance, and the instability of the solid electrolyte interphase (SEI).[17,18] For this reason, a renewed attention has been recently focused towards the fundamental understanding of the sodiation mechanism, aiming at elucidating a direct relation among structural properties of HC and its electrochemical behavior especially by employing operando characterization methods.[10,19–22] However, the controversial nature of the HC structure hinders a comprehensive understanding of the structure-function correlation.[20,22–29]

Several studies have been conducted on the effect of the temperature treatment, the precursor choice and the synthesis method, however, besides the structural and morphological differences of the obtained materials, most of the reported HCs exhibit Na^+ ion storage providing reversible specific capacities ranging between 200–300 $mAh\,g^{-1}$ (further enhanced up to 400 $mAh\,g^{-1}$ by high temperature treatment),[3,30] and ICE within 70–80% (for the best candidates).[31]

In this study instead, we investigate three optimized HCs obtained by using different precursors and synthesis conditions aiming at the obtainment of structurally different HC materials. By comprehensively investigating the derived structural properties we target the identification of the crucial structural properties affecting the electrochemical behavior upon sodiation and lithiation thus assessing the different reactivity of the HCs against the two alkali ions.

The three HCs have been investigated with bulk and surface sensitive techniques facilitating a correlation between their structure and surface chemistry with the resulting electrochemical performance. Furthermore, the sodiation and lithiation behavior of the three HCs has been investigated with a focus on the different surface chemistry involved in the formation and stability of the SEI for Na and Li systems.

Experimental Section

Hard Carbon Material Preparation

Three different HC materials obtained by using different precursors (see Figure S1 in the Supporting Information section) and synthesis processes have been investigated in this study as optimized materials with different structural properties. The first material is a commercial HC (BELLFINE® LN0001, AT Electrode), hereafter defined as c-HC, which was used as received without any further treatment. According to the supplier information, the c-HC powder was obtained by heat treating a phenolic resin precursor at about 1200 °C in N_2 atmosphere. The second material is a polyethylene fiber-derived HC (f-HC), which was obtained by heat treatment of the fiber precursor at 1800 °C in N_2 atmosphere. The fiber precursor was obtained from a melt-spun polyethylene fiber, crosslinked with electron beam treatment with 1000 kGy dosage followed by a 6 h treatment at 250 °C in elemental sulfur under N_2 atmosphere, which converts the polyethylene to a poly(thieno)thiophene polymer. In order to remove the possible sulfur traces from the polyethylene fiber, the carbonization step was carried out at 1800 °C. After the carbonization step, the polyethylene fibers were dry milled via ball-milling in order to make them into powder. The last material is an in-house prepared HC from a lignin-rich biomass precursor, i.e., peanut shells, previously reported and hereafter named as p-HC.[32,33] Briefly, peanut shells were dried at 80 °C, crushed into small pieces (1–3 mm), and treated in a phosphoric acid (PA) solution (85% wt. solution, JT Baker) for 2 weeks. The peanut shell to PA solution weight ratio was 14.8% (25 g peanut shell in 100 mL PA solution). The acid-treated peanut shells were then washed with deionized water until the pH value of 6–7 was reached and further dried at 80 °C overnight. The acid treatment was carried out as an effective method to chemically activate the carbon and incorporate the electrochemically active surface functional groups, as well as the well-developed porous structure as discussed in previous works.[33,34] The pyrolysis step was performed in a tubular furnace (Nabertherm P330) equipped with an alumina tube, at 1100 °C for 1 h under Ar flow (1 $^\circ C\,min^{-1}$ heating rate). The carbonized p-HC was then hand-ground for 30 min in a mortar.

Materials Characterization

The particle size and morphology were evaluated by means of a high-resolution scanning electron microscope (FE-SEM, ZEISS) with acceleration voltage set up to 3 kV. Qualitative elemental analysis was performed with the acceleration voltage of 5 kV by energy dispersive X-ray spectroscopy (EDX, Aztec, Oxford Instruments).

The surface chemistry of the three materials was investigated in detail by means of X-ray photoelectron spectroscopy (XPS), carried out in a SPECS UHV system (FOCUS 500 equipped with monochromatic X-ray source, PHOIBOS 150 hemispherical energy analyzer with 2D DLD detector) using the Al Kα ($h\nu = 1486.6$ eV) radiation (more details in 2.4). The spectra were calibrated to the signal of C-C sp2 at 284.4 eV and analyzed by CasaXPS software.[35] Raman spectroscopy was carried out in a confocal InVia Raman microspectrometer (Renishaw) with a 633 nm red laser and a 50× objective lens in a back-scattering configuration. The spectrum of each HC was collected in the range of 500–3500 cm^{-1} (20 accumulations of 10 sec) and was processed with background removal and normalization by using Origin 2019 software. The deconvolution of the spectra was performed by applying Lorentzian-Gaussian fitting on Spec5 software. The microstructure of the HCs was investigated by WAXS measurements conducted with a RIGAKU D/Max RAPID II using 40 kV and 30 mA with a Cu Kα radiation ($\lambda = 154.059$ nm). The instrument is equipped with a shine monochromator and an image plate detector.

The micro-mesoporosity of the three different HCs was examined on an Autosorb-iQ-MP/XR analyzer (Quantachrome) by Ar physisorption at 87 K. The samples were degassed at 150 °C for 24 h before the Ar isotherms acquisition. The narrow microporosity (micro- and ultramicropores) was also evaluated by CO_2 adsorption at 273 K on an ASAP 2020 analyzer (Micromeritics). For a correct evacuation of the narrower pores, the HCs were firstly degassed at 90 °C for 1 h and, subsequently, to 300 °C for 16 h. The specific surface area (SSA) was calculated according to the multipoint Brunauer-Emmett-Teller (BET) method. The pore size distributions (PSD) were determined by using density functional theory (DFT) method considering Ar and CO_2 adsorption on Carbon Slit Pore models.

Electrode Preparation and Electrochemical Characterization

Electrodes were prepared by mixing 80 wt.% HC active material, 10 wt.% conductive carbon (Super C65, IMERYS), and 10 wt.% carboxymethylcellulose sodium salt (CMC, Sigma-Aldrich). CMC was added as a 2.5 wt.% aqueous solution in deionized water. The mixture was ball-milled in a zirconia jar for 2.3 h (15 min milling and 5 min rest; 7 repetitions; speed of the main disk: 400 rpm; speed of the rotating plates: −800 rpm). Afterward, the blended slurry was casted onto a 10 μm thick battery grade aluminum foil with a wet thickness of 200 μm. The coating was dried at 80 °C overnight under ambient atmosphere and subsequently punched in 12 mm diameter electrodes. The electrodes were dried under vacuum in a glass oven at 120 °C for 20 h. The average mass loading of each electrode was around 1.5 mg cm^{-2}.

The electrodes were employed as working electrodes in Swagelok® T-type cells along with sodium metal (99.8 %, Acros Organics) or lithium metal (battery grade, Honjo) as counter and reference electrodes. 1 M sodium hexafluorophosphate ($NaPF_6$ battery grade, Fluorochem) dissolved in the 1 : 1 (w : w) mixture of ethylene carbonate (EC) and propylene carbonate (PC) (battery grade, UBE) was used as electrolyte solution for the Na-based cells. The commercially available electrolyte solution (UBE) consisting of 1 M lithium hexafluorophosphate ($LiPF_6$) in the 1 : 1 (w : w) mixture of EC and dimethyl carbonate (DMC) was used for the Li-based cells. The electrolyte solutions were soaked into glass fiber separators (GF/D, Whatman). Electrolyte preparation and cell assembly were conducted in an Ar-filled glove box (MB200B ECO, MBraun; H_2O and $O_2 < 0.1$ ppm).

Cyclic voltammetry (CV) tests were performed at a scan rate of 0.1 mV s^{-1} within the 0.02–2.0 V vs. Na^+/Na and Li^+/Li potential range with a multi-channel potentiostat-galvanostat (VMP3, Biologic Science Instruments). Galvanostatic cycling tests were carried out with a battery tester (Series 4000, MACCOR) within the same potential range. A specific current of 200 mA g^{-1} is defined as 1 C. All electrochemical tests were performed on cells stored in climatic chambers at 20 ± 1 °C.

Solid Electrolyte Interphase Characterization

Post-mortem surface analysis was performed by XPS on the pristine HC electrodes and stored 2 h at open circuit voltage (OCV) in contact with the electrolyte solution to analyze the chemical surface reactivity of the different materials. Additionally, surface analysis was performed on HC electrodes from both Na- and Li-based cells at different states of charge (0.02 V and 2.0 V). The measurements were performed using monochromatic Al Kα source (hν = 1486.6 eV) and Phoibos 150 XPS spectrometer with a micro-channel plate and a delay line detector (DLD) in fixed analyzer transmission mode. High-resolution scans were collected at 400 W, 30 eV pass energy, and 0.1 eV energy step. Depth profiling was carried out using a focused ion gun (5 keV Ar^+) for 2.5 and 5 min.

The cycled cells were disassembled inside an Ar-filled glove box. The recovered electrodes were rinsed with diethylene carbonate (DEC) prior to the transfer into the XPS vacuum chamber by using a custom-designed Ar-filled transfer system. The calibration of the binding energy was set on the lithium fluoride (LiF) peak at 685 eV and at the sodium fluoride (NaF) peak at 684.5 eV for the Li and Na cycled electrodes, respectively.[36] Despite being a more commonly used calibration peak, the pseudo-graphitic-like carbon peak at 284.4 eV was not used for calibration reference in this work (except for pristine powders and electrodes). Indeed, the pseudo-graphitic domains are involved in the electrochemical processes, thus the corresponding peak might undergo peak position changes upon cycling. It is well known that Li^+ ions intercalate into the graphite structure forming Li_xC_6, which generally results in a shift to the lower binding energy of the C=C bond.[37] Likewise, it has been recently reported that also the insertion of Na^+ ions into the turbostratically layered pseudo-graphitic nano domain (TLPG-ND) of HCs causes a shift of the peak position.[21] Therefore, selecting the pseudo-graphitic-like peak as a reference for the binding energy calibration would lead to unprecise peak attribution. Instead, LiF and NaF were used as internal calibration for two main reasons, i. e., the binding energy of their peaks is well-known and the peaks do not overlap with other formed species. However, the C=C sp2 peak was used as reference for the pristine electrodes because of the absence of the alkali fluorides. Additionally, no other features overlapping the C=C peak are present in the pristine electrodes.

2. Results and Discussion

2.1. Hard Carbon Powder Characterization

The SEM images in Figure 1 reveal that the morphology, as expected, is strongly influenced by the HC precursor and the synthesis procedure. The micrographs show primary particle size ranging from 2 μm to 5 μm for the c-HC and f-HC materials (see Figure 1a–d), but larger for p-HC (Figure 1e–f). It is evident that the particle size distribution and shape are much more homogeneous for the c-HC when compared to the f-HC and p-HC, due to the more controlled properties of the precursor and the standardized synthesis process. In addition, while c-HC presents well defined spherical particles, f-HC and p-HC exhibit non-homogeneously shaped flake-like particles. Elemental mapping analysis performed by EDX shows that no other chemical species other than carbon and a small amount of oxygen is present in all three HCs (see Figure S2 in the Supporting Information). However, the elemental concentration is slightly different among the three materials, with the f-HC exhibiting the highest oxygen content. Considering the chemical structure of the precursor employed to obtain the f-HC material, i. e., polyethylene fibers (see Figure S1b), it is reasonably assumed that the oxygen species detected through EDX are not sourced by the precursor (oxygen not presented in the structure), but rather from the surface reactivity of the material with the atmosphere after the synthesis process. Indeed, W. Xing et. al. reported that HCs exposed to air after carbonization are more reactive to the charge carriers,[38] hence the oxygen content shown in the HCs studied in this work might be associated with the presence of absorbed oxygen from the atmosphere.

To investigate the surface chemistry of the HCs and the presence of different surface terminal groups, XPS analysis of the powders has been conducted.

Figure 2a–c and d–f present the fitted XPS spectra of C 1s and O 1s core-level spectra of the three HC powders, respectively. The atomic percentage values are summarized in Table 1, while the relative concentration of each C- and O-containing chemical species for each spectrum is listed in Table S1.

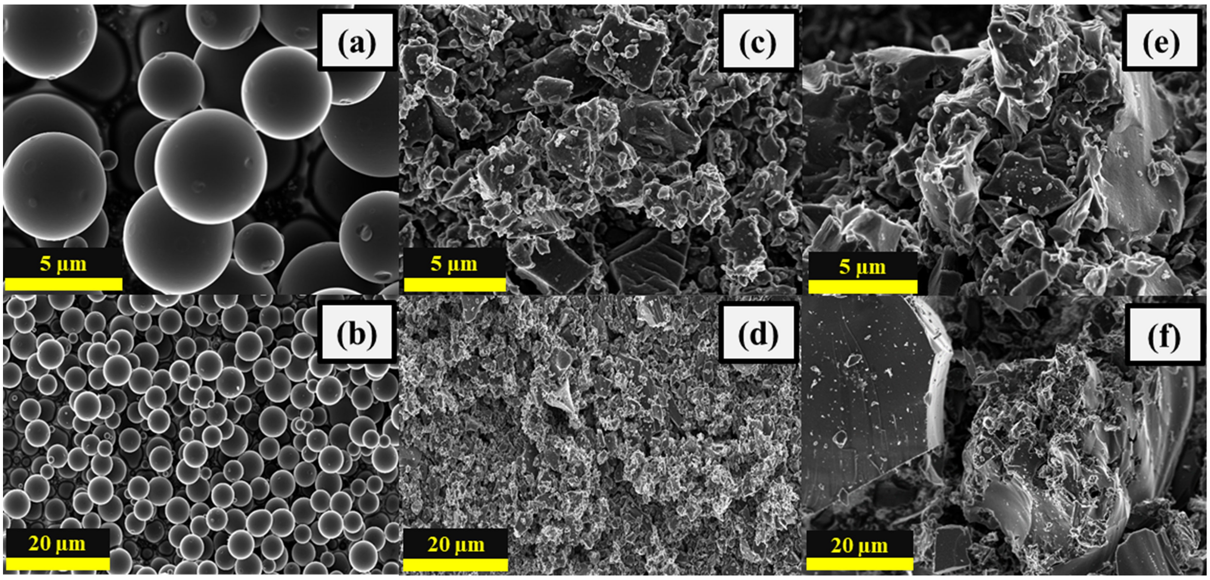

Figure 1. SEM images of HC powders: a, b) c-HC, c, d) f-HC, and e, f) p-HC.

Table 1. Observed and calculated structural properties of HC powder samples obtained by different analytical techniques including XPS, EDX, Raman spectroscopy, WAXS, and Ar and CO_2 adsorption measurement.

	c-HC	f-HC	p-HC
XPS survey analysis [at.%]	C: 93.44 O: 6.56	C: 90.06 O: 9.94	C: 90.43 O: 9.57
EDX Analysis [at.%]	C: 99.03 O: 0.97	C: 97.67 O: 2.33	C: 98.42 O: 1.58
A_D/A_G – area ratio (Raman)	3.30	2.67	3.59
Calculated L_a (Raman) [nm]	11.68	14.43	10.73
Calculated d_{002} (WAXS) [nm]	0.38	0.36	0.38
Calculated L_a (WAXS) [nm]	4.23	4.51	3.43
Calculated L_c (WAXS) [nm]	0.95	1.20	0.93
$R_p=I_{peak}/I_{BG}$(WAXS)	2.89	4.46	2.34
Average n. graphene layers per stack (WAXS)	2.47	3.37	2.43
BET surface area (Ar ads.) [$m^2\,g^{-1}$]	7	150	3

The trend of the atomic concentration of C and O is in good agreement with the EDX results, with c-HC having the highest carbon content among all, and f-HC showing the highest concentration of oxygen. While the trend is similar, the absolute values of C and O content obtained with EDX and XPS analysis are different most likely due to the fact that XPS is limited to the surface region (max. 10 nm), while EDX probes a higher penetration depth of few micrometers. The higher oxygen amount observed by XPS suggests that most of the O-containing species are concentrated at the surface of the materials. Regarding the carbon species, despite that the C 1s spectra of three HCs are very similar in shape, the relative concentration of chemical species obtained by fitting is rather different. Despite it is expected that f-HC contains more C=C sp2 species due to the highest carbonization temperature, the c-HC sample shows the highest concentration of C=C sp2 species, suggesting an inferior amount of chemical species on its surface. The fact that f-HC contains more surface terminal groups, as confirmed by the high oxygen (see EDX results) and C–O/C=O, and O–C=O amount (see Figure 1e and Table S2) and EDX results, can indeed hinder the detection of the underlying pseudo-graphitic-like sp2 carbon network.

The Raman spectrum of disordered carbon material like HCs, normally exhibits a broad peak at around 1340 cm^{-1} called D-band, and a sharper peak at about 1580 cm^{-1} referred to G-band. According to Sadezky et. al., the spectrum of disordered carbon materials can be deconvoluted into five components,[39] including the D- and G bands, and the D′-, D3-, and D4 bands. The D band is generally induced by the vibrational mode of defected/disordered graphitic lattice ring breathing, hence also known as a disorder-induced band. The G band is associated with the vibrational mode of in-plane bond-stretching motion of all sp2 atoms in the aromatic ring in the graphitic lattice. D′ band is another lattice vibration of the surface graphene layers, namely, the graphene layers which are not directly neighbouring with other graphene layers as in the case of graphite.[39] D3 band located around 1500 cm^{-1} is commonly associated with the vibrational response of the amorphous carbon content such as adsorbed molecules, molecular fragments, or functional groups. Finally, the small shoulder of the D band in the lowest

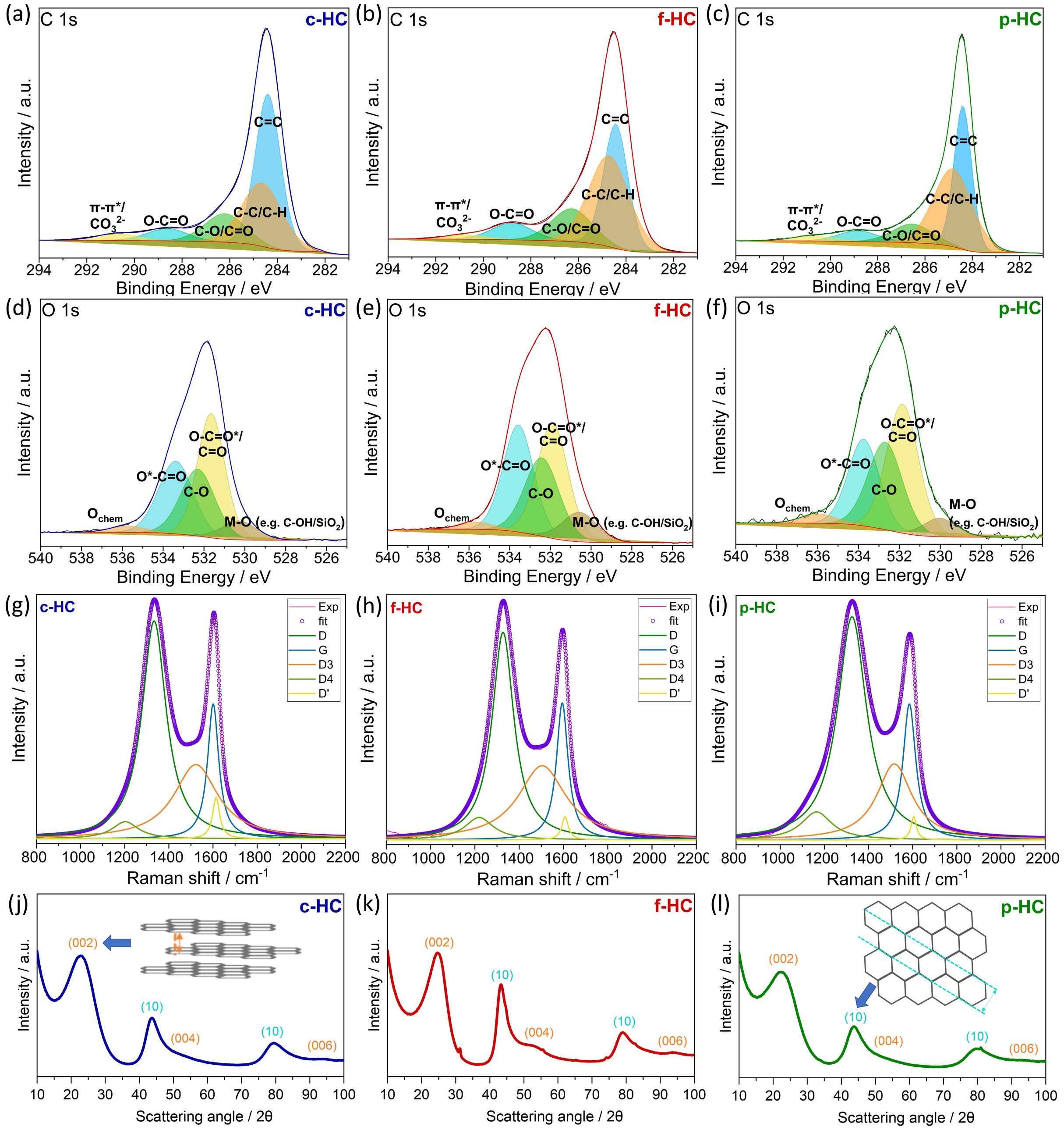

Figure 2. C 1s core-level for a) c-HC, b) f-HC, c) p-HC, and of O 1s core-level for d) c-HC, e) f-HC, f) p-HC. De-convoluted Raman spectra for g) c-HC, h) f-HC, and i) p-HC. 2D plot of WAXS patterns for j) c-HC, k) f-HC, and l) p-HC.

wavelength denoted as D4 is attributed to sp2–sp3 bonds or C=C/C–C stretching motions in polyene-like structures.

The curve fitted Raman spectra of each HC powder are presented in Figure 2g–i. In Figure 2g, an intense contribution of the D′ band to c-HC on the overall peak located at around 1600 cm^{-1} indicates that c-HC contains a higher concentration of surface graphene layers in accordance with the XPS results. The p-HC (see Figure 2i), on the other hand, seems to have a higher degree of disorder than the other two HC samples as suggested by the high intensities of the D- and D4 bands. Thus, it is reasonably assumed that the p-HC contains a larger proportion of crosslinked-like moieties on the defects of the TLPG-ND than the other two HCs.

Two important structural parameters can be calculated from Raman spectra. The first one is the degree of disorder which can be estimated by calculating the I_D/I_G ratio. The second one is the in-plane crystalline size which can be calculated according to the Tuinstra Koenig's relation[40] as reported in Eq. (1).

$$L_{a,\,\mathrm{Raman}}\ [\mathrm{nm}] = (2.4 \times 10^{-10}) \cdot \lambda^4 \cdot \left(\frac{I_D}{I_G}\right)^{-1} \tag{1}$$

For carbons with high defect concentration, the I_D/I_G can be calculated by considering the area ratio (A_D/A_G) rather than the intensity ratio due to the variation of the peak width.[41] The calculated A_D/A_G ratios are 3.30, 2.67, and 3.59 and the in-plane crystallite size ($L_{a,\ \mathrm{Raman}}$) is 11.68 nm, 14.43 nm, and 10.73 nm for c-HC, f-HC, and p-HC, respectively (see Table 1).

As expected, the A_D/A_G ratio decreases with increasing crystallite size which is directly proportional to the pyrolysis temperature. The p-HC shows the higher A_D/A_G value indicating a higher degree of disorder, and in agreement with the higher contribution of the D- and D4 bands. Whereas the f-HC exhibits the lowest A_D/A_G ratio and the largest crystallite size owing to its larger proportion of the ordered structure of graphene layers resulted from the extremely high carbonization temperature adopted during the synthesis process, i.e., 1800 °C, suggesting that the degree of disorder seems not so dependent on the precursor, but rather on the pyrolysis temperature.

Although the detailed microstructure of HC is still hard to be defined, it is generally accepted to consider that non-graphitic carbons contain turbostratic stacks of small graphene layers in the nanometer range. Despite the highly disordered microstructure of HC, the degree of order of the material can be estimated by determining the average dimensions of these stacks, which can be calculated through WAXS measurements (stack height $L_{c,\ \mathrm{WAXS},}$ and interplanar crystallite size $L_{a,\ \mathrm{WAXS}}$) .[42] The WAXS powder patterns of the three HCs are displayed in Figure 2j–l. The spectra show the typical features of disordered carbons including the symmetric (00 *l*) reflections linked to the parallel stacking of carbon layers (interlayer scattering) and asymmetric (*hk*) reflections associated with the 2D internal structure of the layers (intralayer scattering).[43,44] The line profiles of the two reflections are often used to evaluate the size and disorder parameters of its corresponding carbon layers. For instance, the increasing width of the line profile indicates a higher degree of lattice imperfection. Furthermore, according to Dahn et. al., the number of graphene layers stacked in parallel can be roughly estimated by calculating the R_p ratio which is defined as the ratio between the peak height of the (002) reflection over the background height at the peak position.[45]

The calculated R_p values obtained for the three HCs are reported in Table 1, and the peak fitting information is listed in Table S2. The calculated R_p values are 2.89, 4.46, and 2.34 for c-HC, f-HC, and p-HC, respectively, indicating again (in good agreement with the calculated A_D/A_G ratio) a higher degree of graphitization of the f-HC (higher number of parallel stacked graphene layers). Besides, the pronounced (002) and (10) reflections observed for the f-HC (see Figure 2k) suggest a higher degree of graphitization due to the highest carbonization temperature used during the synthesis. The p-HC, on the other hand, shows a higher degree of defects in its structure as indicated by the broad and low intensity reflections, in agreement with the highest A_D/A_G ratio and the lowest R_p.

Finally, the analysis of the spectral parameters enables the determination of the average interlayer spacing d_{002} from Bragg's equation [Eq. (2)], and the stacking height L_c and the interplanar crystallite size L_a with Scherrer's equation [Eq. (3)].

$$n\lambda\ [\mathrm{nm}] = 2d_{002} \cdot \sin\theta_{002} \tag{2}$$

$$L_{\mathrm{a\ or\ c,WAXS}}\ [\mathrm{nm}] = \frac{K_S \cdot \lambda}{\beta \cdot \cos\theta} \tag{3}$$

Where K_S is a shape factor, λ is the wavelength of the X-ray source, β is the full width half maximum (FWHM) of the line profile of the corresponding peak and θ is the diffraction angle. The shape factors K_s of disordered carbon are 0.89 and 1.84 for L_c and L_a, respectively.[46] The calculated crystallite sizes of the three HCs are reported in Table 1. Due to the similar diffraction angle and FWHM of the (002) reflection of c-HC and p-HC (see Table S2), rather similar average interlayer spacing and comparable inter-planar crystallite size are obtained for these two HCs. Whereas a smaller interlayer spacing and a larger interplanar crystallite size are observed for f-HC due to its exceptionally high pyrolysis temperature (1800 °C). The planar crystallite size from the WAXS measurements can be compared to the calculated crystallite size obtained from the A_D/A_G ratio of the Raman spectra. Both calculated values present the same trend, with f-HC having the largest crystallite size followed by c-HC and p-HC, respectively. Note that the calculated L_a values from WAXS are lower than the L_a from Raman due to the characteristic principle of the X-ray scattering technique as reflecting the interplanar layers which are parallelly oriented[47] as well as the turbostratic nature of HC experiencing peak broadening in WAXS analysis influenced by other structural parameters such as strains and layer curvatures.

The porosity of the HCs was examined with gas physisorption by using two different probe gases, i.e., Ar (87 K) and CO_2 (273 K) for micro-mesoporosity and ultramicroporosity, often referred to as "open porosity" and "closed porosity", respectively. The associated isotherms and pore size distributions (PSDs) are reported in Figure 3. N_2 (77 K) adsorption measurements have also been performed, however, with unreliable results except for f-HC, most likely due to the very narrow pores or the narrow path to reach them. Moreover, it is worth noting that due to the possible interaction of the N_2 quadrupole on the surface of the adsorbent, IUPAC recently suggested using Ar as the probe gas (instead of N_2) for a more accurate and comprehensive pore structural analysis.[48–50] Nonetheless, owing to the intrinsic limited diffusion of Ar molecules into ultramicropores (pore width <0.7 nm), CO_2 was used as an adsorptive at elevated temperature (273 K) in the low relative pressures ($P/P_0 < 0.03$) according to the IUPAC recommendations. Thus, in this study, both Ar and CO_2 adsorption characteristics were investigated for a comprehensive pore structure analysis of the complex HC micropore structure.

Figure 3a and 3b show the Ar and CO_2 adsorption isotherms, respectively. f-HC shows a distinctively high adsorbed volume of Ar at low relative pressures (SSA of 150 $m^2\,g^{-1}$, Table 1) which indicates, in principle, a larger micropore volume compared with c-HC and p-HC. A type II isotherm with a slight slope in the medium-high relative

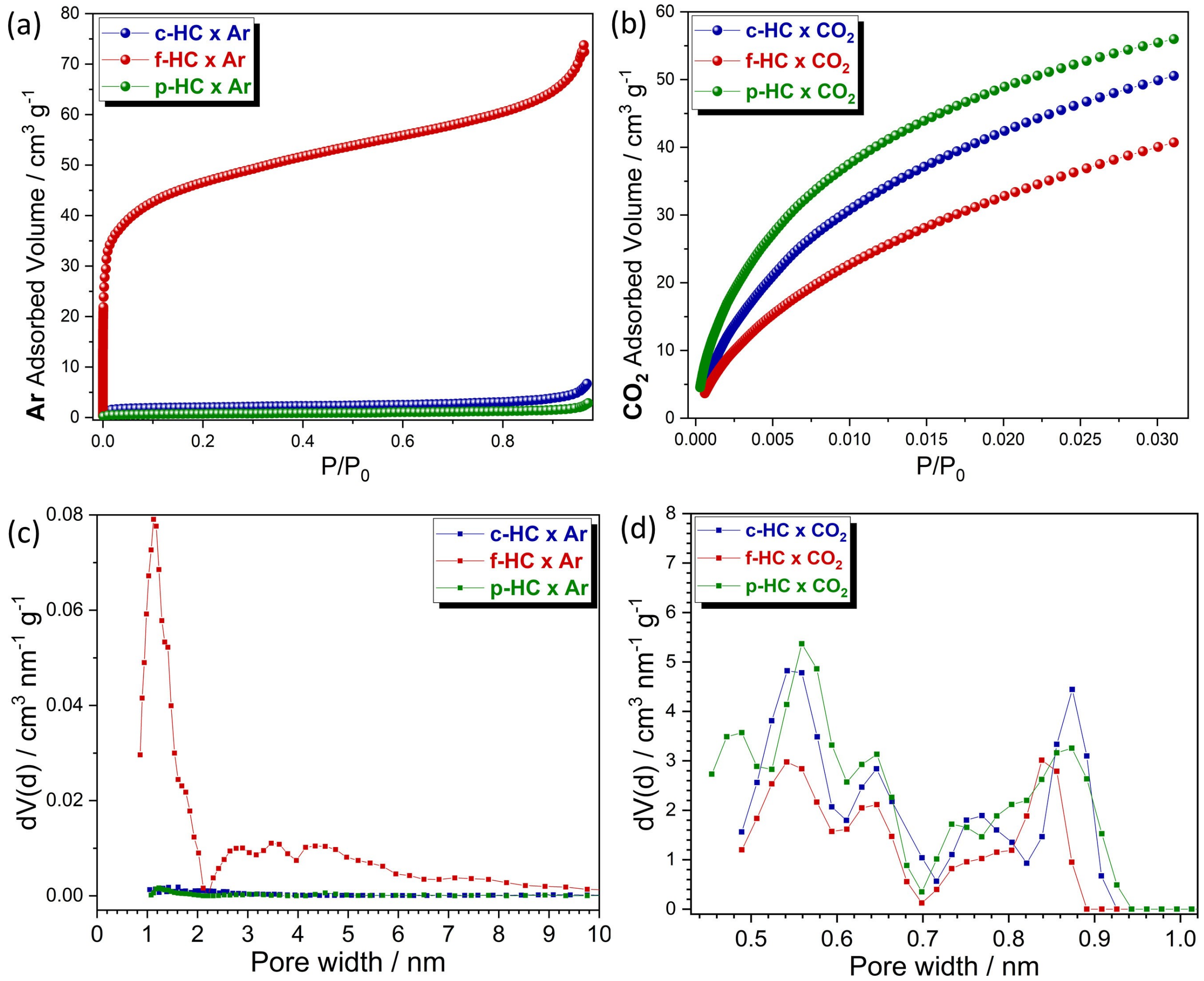

Figure 3. Gas adsorption isotherms with different probe gases: a) Ar adsorption, b) CO_2 adsorption, and corresponding pore size distribution: c) micropore size distribution determined by Ar adsorption based DFT calculation and d) ultramicropore size distribution determined by CO_2 adsorption based DFT calculation.

pressures also reveals the presence of mesopores in f-HC. These larger pores are verified by the PSDs (Figure 3c), where f-HC presents a wide maximum between 2 and 6 nm. According to Dahn et. al.'s "falling cards model", the turbostratically oriented graphene-domains in HC fall into parallel orientation to their neighboring domains when provided with efficient thermal energy and generate bigger voids.[45] Given the high pyrolysis temperature used for f-HC larger sized bulk pores are expected. On the other hand, c-HC and p-HC exhibit almost negligible adsorbed volumes of Ar. The Ar PSD for f-HC (Figure 3c) displays a maximum centered at 1 nm and an additional contribution of mesoporosity, whereas the Ar PSD of c-HC and p-HC confirms no presence of mesoporosity and an insignificant amount of microporosity.

Interestingly, the CO_2 isotherms show a completely reversed trend in respect to the Ar isotherms (Figure 3b). The p-HC is the material displaying the higher amount of adsorbed CO_2 (SSA of 292 $m^2 g^{-1}$), even though the difference in the adsorbed volume among all HCs is not as significant as in the case of Ar. The CO_2 isotherm of f-HC has a more linear character at relative pressures below 0.01, which indicates a lower amount of narrow micropores (ultramicropores) as compared with the other two HCs. In fact, the CO_2 PSDs for both c-HC and p-HC display a larger volume of pores below 0.7 nm (Figure 3d).

As targeted, given the different synthesis conditions adopted for the obtainment of the three materials, very different structural properties have been obtained. In the next section, all the above-mentioned structural differences detected for the three HCs will be considered when discussing the different electrochemical performances upon Na and Li storage assessing a structure-function correlation.

2.2. Electrochemical Behavior of HC Anodes Upon Na and Li Storage

Figure 4 presents the CV curves recorded for the three HCs upon Na (Figure 4a–c) and Li (Figure 4d–f) uptake and release.

Overall, a clear difference is observed between the Na and Li half cells. While the HCs exhibit a rather reversible sodiation/

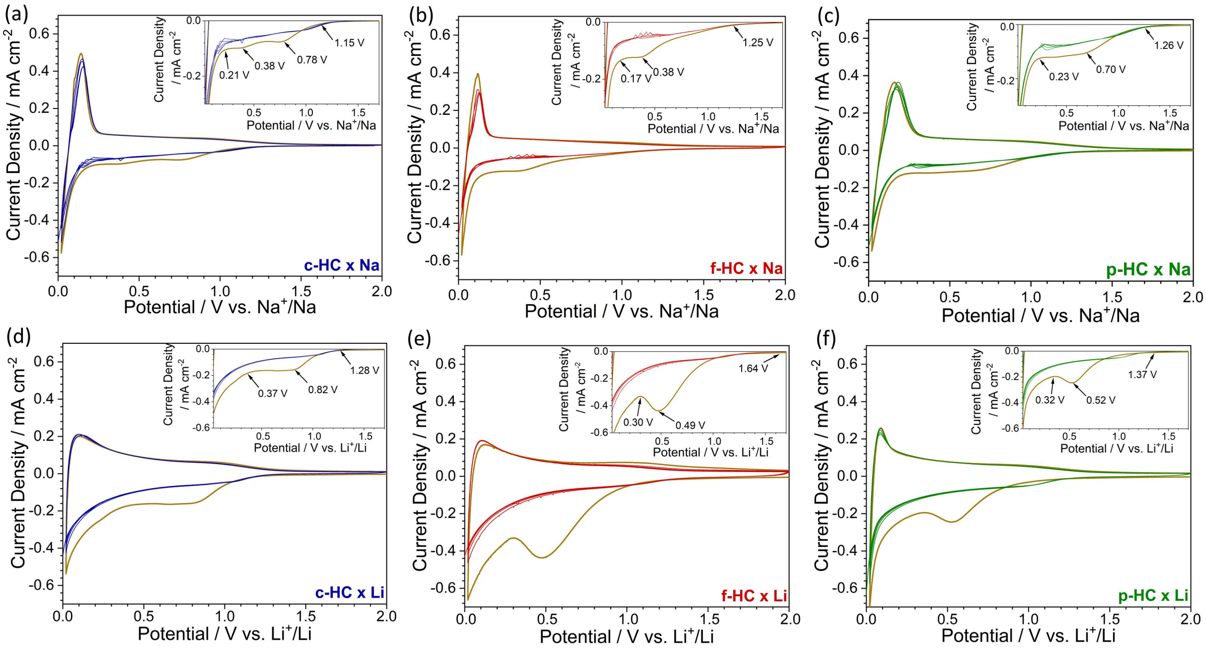

Figure 4. CV curves of a) c-HC, b) f-HC and c) p-HC in Na cells. Electrolyte: 1 M $NaPF_6$ in EC : PC (1 : 1 wt.%), scan rate: 0.1 mV s^{-1}, potential range 0.02–2.0 V vs. Na^+/Na. CV curves of d) c-HC, e) f-HC and f) p-HC in Li cells. Electrolyte: 1 M $LiPF_6$ in EC : DMC (1 : 1 wt.%), scan rate: 0.1 mV s^{-1}, potential range 0.02–2.0 V vs. Li^+/Li. Insets report the electrolyte decomposition potential regions.

de-sodiation reaction upon cycling, as demonstrated by the two sharp peaks at low potential, they display similar lithiation degree, but with higher irreversibility in the de-lithiation process.

The three HCs upon Na uptake and release (Figure 4a–c), reveal similar profiles in the first and following cycles. The first cathodic scan (see gold curves) unfold three main processes. The first one occurring between 2.0 V and 1.2 V is generally attributed to the storage of Na^+ ions at defect sites and surface terminal groups. The second one, from 1.2 V until 0.3 V associated with the electrolyte decomposition reaction and SEI formation[51] and the third one with much higher current densities at potentials lower than 0.3 V is attributed to the Na^+ ion storage into the carbon structure of both the HC and the carbon additive.[12,23] Among the three HCs, f-HC presents higher current densities during the first cathodic scan in the electrolyte decomposition potential region, suggesting an increased electrochemical reactivity towards the electrolyte, i.e., the formation of a thicker SEI, with consequent poor ICE. In the low potential region, however, a rather similar amount of charge is consumed during the sodiation process for all the HC electrodes. During the following anodic scan, f-HC and p-HC exhibit slightly lower current densities for the de-sodiation process when compared to c-HC suggesting a higher amount of irreversible sodium trapping, which can be also related to thicker and/or inhomogeneous SEI formation. Moreover, p-HC exhibits also a broader de-sodiation peak indicating a slower kinetic of the sodiation/de-sodiation reaction when compared to the faster de-sodiation process observed for c-HC and f-HC. The slower sodiation kinetic of p-HC might be associated to the highest concentration of defects observed in p-HC compared to c-HC and f-HC as detected by Raman spectroscopy.

Very different behavior is observed upon lithiation (Figure 4d–f). All three HC electrodes exhibit inferior reversibility of the Li uptake and release compared to Na. The first cycle particularly varied the most among the three HCs. The f-HC triggers an extensive electrolyte decomposition as indicated by the broad peak at around 0.5 V followed by p-HC and c-HC. It is expected that the difference in the first cathodic scan will result in a great variation of the SEI thickness in the Li cells. Besides, the lithiation process occurring below 0.3 V presents rather sluggish kinetics compared to the sodiation as indicated by the broad peaks. Among them, the p-HC presents the sharpest peak and the highest current density involved in the de-lithiation process (anodic scan) suggesting for its improved electrochemical behavior compared to the other HCs.

The CV profiles also demonstrate a clear difference in the performance of the three HCs with the two investigated alkali ions. The differences may be attributed mainly to the surface reactivity of the HCs with the electrolyte (SEI formation and stability), but also to their structural properties, which offer different domains and reactive sites for the Na^+ and Li^+ ion interaction. Moreover, the pore structure and size certainly play a key role in the electrochemistry of the three systems. Indeed, depending on their shape and size, pores could appear as open or closed to Li^+ or Na^+ ions. Considering the difference in the ionic size, the ultramicropores could appear open to Li^+ ions and contribute to the increased first irreversible capacity loss, which is known to be proportional to the concentration of open porosity in the structure.[17]

The electrochemical behavior upon sodiation and lithiation has been further investigated by galvanostatic cycling tests. Figure 5a and 5d illustrate the first galvanostatic cycle of the three HCs upon uptake and release of Na and Li, respectively.

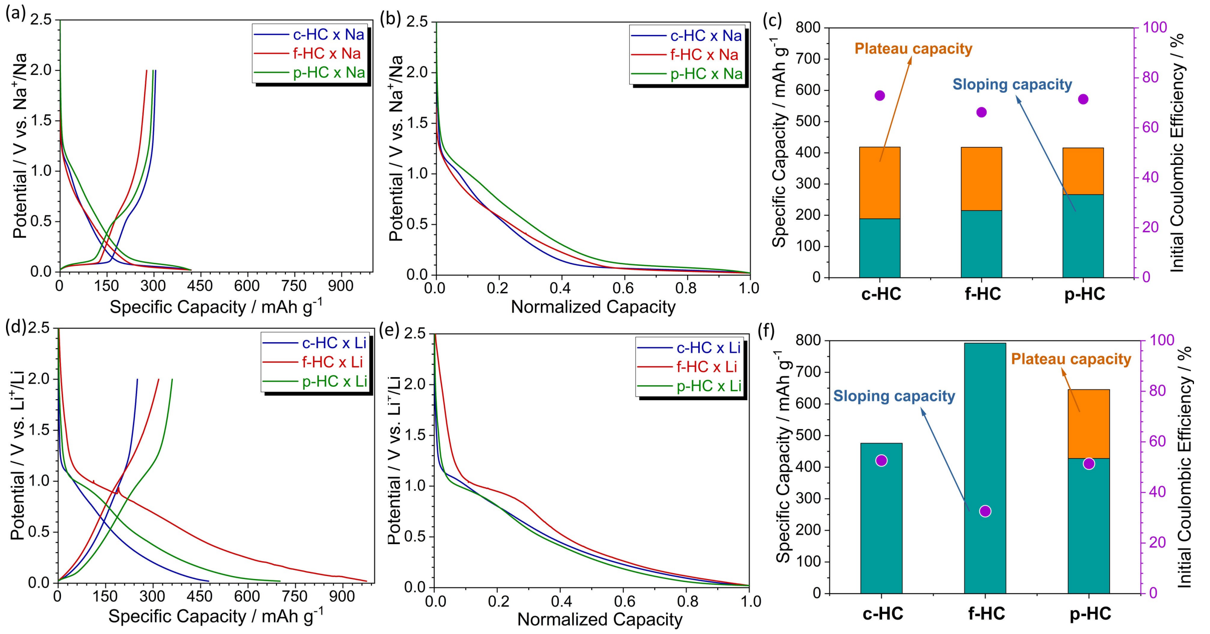

Figure 5. Comparison of the first cycle potential profile and corresponding normalized first cycle discharge capacity for c-HC, f-HC and p-HC cycled at 4 mA g^{-1} in a, b) Na cell using 1 M $NaPF_6$ in EC:PC (1:1 wt.%) electrolyte (potential range 0.02–2.0 V vs. Na^+/Na) and d, e) Li cell using1 M $LiPF_6$ in EC:DMC (1:1 wt.%) electrolyte (0.02–2.0 V vs. Li^+/Li). Capacity contribution from the sloping and plateau regions during the first discharge of the HC electrodes in c) Na cell, and f) Li cell.

The corresponding normalized potential profiles upon Na and Li uptake are shown in Figure 5b and 5e, respectively. The capacity distribution between the high potential and the low potential region as well as the ICE is reported in Figure 5c (for Na) and Figure 5f (for Li). Regardless of the tested HC, it is evident that the potential profiles obtained upon Na^+ or Li^+ ion uptake and release are very dissimilar as already observed from the CV experiments. Indeed, the lithiation process evolves mainly through a continuous sloping potential profile, while the sodiation process exhibits an initial sloping region followed by a distinct plateau below 0.1 V. This behavior has been previously observed and explained by DFT simulations.[52] It was also suggested that, a plateau-like potential profile could appear upon lithiation only when an extremely low current is applied (slow reaction kinetics).[52]

The exceptional trace of the plateau-like low potential profile of p-HC upon lithiation compared to the other two HCs suggests for an additional Li^+ ion storage process. This can be explained by the high defect concentration observed for p-HC (see Raman data in Figure 2i). Indeed, it is well known that defects in the pseudo-graphitic domains acts as electron-rich spots where ions are preferentially adsorbed. For p-HC, the defects are interacting with Li^+ ions at an early stage of lithiation, most likely during the sloping region. The reacted defects may delay further lithiation, thus leading to slower kinetics of lithiation which may cause the appearance of the low potential feature. However, an effect of the particle size cannot be neglected. Indeed, p-HC exhibits the largest particles, which may induce slower lithiation kinetics.

The 1st cycle irreversible capacity of c-HC, f-HC, and p-HC is, respectively, 113, 141, and 118 mAh g^{-1} upon sodiation, and 225, 656, and 340 mAh g^{-1} upon lithiation, suggesting the enhanced reversibility of the sodiation process and a higher degree of irreversible electrolyte decomposition upon lithiation, in accordance with the CV curves. Interestingly, f-HC exhibits the largest irreversible capacity in both systems. This is most likely due to the more accessible ultramicropores by the electrolyte resulting from the presence of mesopores, which promote a higher degree of surface reactivity. Although the first sodiation capacity is very similar for all HCs, some differences in the capacity distribution are observed in the sloping and plateau regions (see normalized discharged capacities in Figure 5b). c-HC offers the largest capacity contribution in the plateau region (~55%), while p-HC displays the highest contribution in the sloping region (64%). Finally, f-HC shows a similar contribution to the overall capacity of the two potential regions (see Figure 5c).

The varying capacity distribution of the HCs between the two regions is associated with the different structural and surface properties of the materials affecting the Na^+ ion storage (adsorption/insertion) mechanism. Indeed, c-HC shows the lowest number of defects and surface terminal groups resulting in the lowest capacity contribution into the sloping region. In addition, the highest concentration of the surface graphene layers, as well as the 2nd largest degree of structural order and ultramicroporosity of c-HC, collectively promotes the highest capacity observed into the plateau region when compared to the other HCs. On the other hand, f-HC showing the highest concentration of surface terminal groups and the largest fraction of micro- and mesopores, results in the 2nd biggest contribution of capacity into the sloping region as well as the lowest ICE. However, it is worth noting that even though f-HC shows the highest degree of structural ordering and the largest crystallite size, not particularly extended plateau region is observed. This can be explained considering the small interlayer distance, the low ultramicroporosity and defects. Indeed, according to Yusuke et. al., 0.36 nm is the limiting threshold for Na^+ ions insertion in the pseudo-graphitic domains[26] and the calculated average interlayer distance for f-HC is at the threshold (0.36 nm, see Table 1). In addition, the lowest ultramicroporosity is observed for f-HC, which would eventually limit the plateau capacity. Also, a low concentration of defects is observed which does not slow down the lithiation kinetic (as instead observed for p-HC). Finally, the highest capacity contribution to the sloping region for p-HC can be attributed to the highest concentration of defect sites in the TLPG-ND as suggested by Raman analysis and to the 2nd largest amount of surface terminal groups. The lower capacity contribution to the plateau region is mainly due to the lowest degree of structural ordering. However, considering the similar interlayer distance, A_D/A_G ratio, and ultramicroporosity for c-HC and p-HC, not having a similar plateau capacity might infer the interconnection between the Na^+ ion storage at the TLPG-ND and ultramicroporosity. It seems that the c-HC's structure, with fewer defect sites in its TLPG-ND, facilitates the transfer and insertion of ions into the domain and ultramicropores. While the larger amount of defects in the p-HC's structure could kinetically hinder Na^+ ions storage in the TLPG-NDs and ultramicropores.

Remarkable differences are observed among the three HCs upon Li uptake and release (see Figure 5d). The corresponding normalized discharge capacities are reported in Figure 5e. c-HC and p-HC show a rather similar potential versus normalized lithiation capacity (Figure 5e) with an initial sudden drop to around 1 V. On the other hand, f-HC already shows Li-storage capacity from 2.0 V. Overall, c-HC and p-HC exhibit similar capacities, but f-HC showed a much higher sloping capacity with lower ICE, even when compared to the f-HC electrode upon sodiation. This can be associated with the more extensive electrolyte decomposition occurring upon lithiation (higher reactivity triggered by the "higher" open porosity available to Li^+ ions compared to Na^+ ions).

The capacity distribution upon lithiation (see Figure 5f) has been split by considering the capacity delivered above and below 0.1 V, which is generally accepted to be the changing point from the sloping to the plateau region in the potential profiles.[53] This enables a comparison of the results upon sodiation, even though a clear plateau below 0.1 V cannot be observed upon lithiation.

The largest plateau-like capacity showed by p-HC upon lithiation is in good agreement with the CV result and most likely related to the highest number of defects, the higher degree of disorder, and ultramicroporosity filled by the electrolyte as explained previously. Interestingly, the ICE values, which are directly related to the irreversible Na trapping during SEI formation, are rather different upon Na and Li uptake and release, most likely due to the higher reactivity of the HCs with the Li-based electrolyte. On the other side, the differences between the three HCs can be directly related to the SSA and microporous structure as will be discussed in section 3.3.

The cycling behavior at 20 $mA\,g^{-1}$ for the three HCs in Na and Li cells, is displayed in Figure 6a and 6b, respectively. The potential profiles of selected cycles (1st, 5th, 20th, and 50th) are reported in Figure S3. The electrochemical parameters extrapolated from the galvanostatic cycling tests are summarized in Table 2. In general, the sodiation of HCs exhibits better stability upon cycling than lithiation, as evidenced by the capacity retention trends over 50 cycles.

Except for f-HC, c-HC, and p-HC show pretty stable electrochemical performance after the initial few Na uptake and release cycles, suggesting the formation of a stable SEI already before the 10th cycle. The f-HC, instead, after showing a substantial capacity loss over the initial 10 cycles, slowly recovers and even improves its reversible capacity upon cycling. Likewise, upon lithiation all HCs need more than 10 cycles to provide stable reversible capacities and satisfactory CEs. This is expected to result in thicker or less stable SEI (dissolving/forming upon cycling), owing to the continuous electrolyte decomposition associated with the poor passivating properties of the formed SEI and/or the enhanced surface reactivity of the HCs toward the Li-based electrolyte.

The different features in the potential profiles and cycling performances confirm that the same HC electrode behaves differently towards the carrier ions due to their structural and surface properties. Indeed, the capacity distribution over the sloping and plateau region upon sodiation is rather different among the three HCs, while a more similar behavior is observed upon lithiation. This might suggest that the interlayer spacing and/or concentration/size of the micro-/ultramicroporosity are more influential for the Na^+ ion storage. Mean-

Table 2. Comparison of galvanostatic cycle performances significant values of HC electrodes in Na and Li cells.

Na cells	1st DC [$mAh\,g^{-1}$]	1st CC [$mAh\,g^{-1}$]	1stcycle CE [%]	2nd DC [$mAh\,g^{-1}$]	2nd CC [$mAh\,g^{-1}$]	Average η_{CB} [%]	Capacity retention (2nd vs. 50th cycle [%])
c-HC	418.63	305.27	72.92	318.73	303.99	99.78	89.57
f-HC	417.81	276.71	66.23	265.86	244.97	98.74	97.80
p-HC	415.84	297.16	71.46	297.87	285.08	99.47	95.52
Li cells							
c-HC	475.68	250.36	52.63	244.01	220.13	98.37	82.94
f-HC	974.54	317.65	32.60	313.03	258.97	98.13	68.17
p-HC	701.34	360.45	51.39	322.04	271.16	97.24	70.42

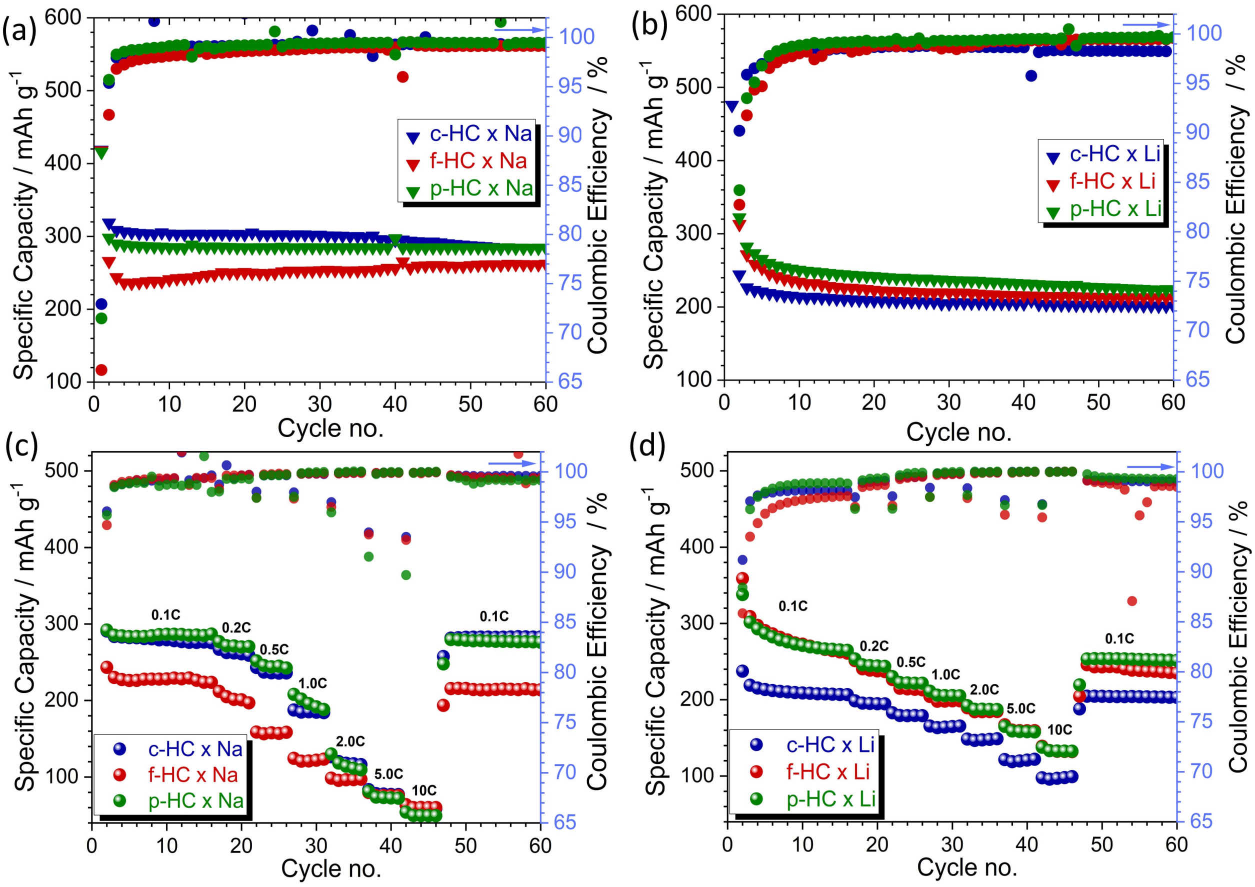

Figure 6. Cycling performances of galvanostatically cycled HC electrodes starting at 4 mA g^{-1} as a low current activation cycle, followed by 20 mA g^{-1} long term cycling in a) Na cells using 1 M NaPF$_6$ in EC:PC (1:1 wt.%) electrolyte (potential range 0.02–2.0 V vs. Na$^+$/Na), and b) Li cells using 1 M LiPF$_6$ in EC:DMC (1:1 wt.%) electrolyte (0.02–2.0 V vs. Li$^+$/Li). Rate performances of galvanostatically cycled HC electrodes in c) Na, and d) Li cells. The cells were firstly cycled at 4 mA g^{-1} as an activation cycle, and later at 0.1 C, 0.2 C, 0.5 C, 1.0 C, 2.0 C, 5.0 C, and 10 C in the potential range of 0.02–2.0 V (vs. Na$^+$/Na and vs. Li$^+$/Li).

while, upon lithiation very low ICE (compared to sodiation) and large capacity fading are observed, suggesting that the micro-mesoporosity is the most influential parameter for Li$^+$ ions storage, especially in the sloping region. Instead, the interlayer spacing does not strongly affect the Li$^+$ ion storage mechanism. On the other hand, structural properties such as defects along with the high overpotential close to the plating potential can instead induce slower insertion kinetics like in the case of p-HC, enabling additional insertion at very low potential values.

Lastly, the rate capability of HC anodes in both systems is displayed in Figure 6c and 6d. As previously depicted in the cycling tests, the sodiation process seems to stabilize faster than lithiation in the initial cycles at 0.1 C. Upon sodiation (see Figure 6c), c-HC and p-HC deliver similar capacities at different current densities, as expected from the cycling performance. However, the capacity extensively drops from 1.0 C to 2.0 C, and translates into the loss of the low potential plateau as displayed in Figure S4a and S4e, which can be explained by the slow kinetics induced by defects and particle size. The capacity fade of p-HC is slightly more severe than c-HC at high current densities, most likely due to the higher degree of disorder blocking the accessibility (insertion) of the charge carriers and to particle size effect. At the same time, the filling of the ultramicropores results to be a kinetically hindered process at such high current densities. Whereas the f-HC already loses its plateau capacity already at 1 C enabling preferential Na$^+$ ions adsorption at energetically favored defects and heteroatoms (contributing to the sloping region capacity).

On the other hand, the rate capability of the HCs upon lithiation follows the same trend as in the long-term cycling (Figure 6d). f-HC and p-HC deliver similar capacities (and their fading) at different current densities. However, p-HC exhibits a superior recovery of the capacity, which can be attributed to a more stable SEI layer. Meanwhile, c-HC shows a more stable capacity at 0.1 C, but overall lower specific capacities at all current densities. This is related to the lowest concentration of defects and surface terminal groups, which contribute to the capacity delivered in the sloping region.

2.3. Solid Electrolyte Interphase Characterization

To elucidate the different surface chemistry and reactivity of the HCs toward the electrolyte, *ex-situ* XPS analysis of electrodes taken from both the Na and Li cells at different states of charge (SOC) during the first galvanostatic cycle, has been performed.

The SEI formation upon sodiation on the surface of the HCs and its evolution (at OCV, sodiated state at 0.02 V, and de-sodiated state at 2.0 V) (Figure 7) was examined by analyzing the C 1s, Na 1s, F 1s, and P 2p photoelectron lines. The SEI formation and its chemical composition on the three HCs at different SOC are similar, but the concentration of the formed species varies.

The C 1s photoelectron line (see Figure 7a) shows that at OCV, all HCs present a component at 284.4 eV corresponding to the pseudo-graphitic network (C═C). Towards high binding energies, the presence of C–C and C–H bonds (285.0 eV, also named as hydrocarbons) from HC and atmospheric contamination is also observed. At even higher binding energies, oxidized carbon species are seen, which correspond to carbon surrounded by one (C–O at 287 eV), two (O–C═O at 288.5 eV), and three (CO_3^{2-} at ~290.2 eV) oxygens.[54] These species are also observed in the pristine electrodes (see Figure S5 and Table S3), indicating that they are most likely due to the reaction with atmospheric oxygen as well as the presence of CMC binder (C–O bond signal). However, the intensity of C–C/C–H and oxidized species peaks increases with respect to the C═C peak at OCV than for the pristine electrode. Therefore, this suggests that these species are formed to a larger extent during the OCV period, indicating the occurrence of spontaneous chemical reactions at the HCs' surface with the electrolyte even in the absence of an applied current. The spontaneous chemical reactivity was also previously observed for several anodic and cathodic materials in Na metal cells. This was attributed to the electrode cross-talking because the highly reactive Na metal promotes the formation of reduced species in the electrolyte later interacting with the electrode material under investigation.[55–58]

At the sodiated state (0.02 V), the pseudo-graphitic network signal (C═C) decreases in all HCs. The same occurs to the C–O

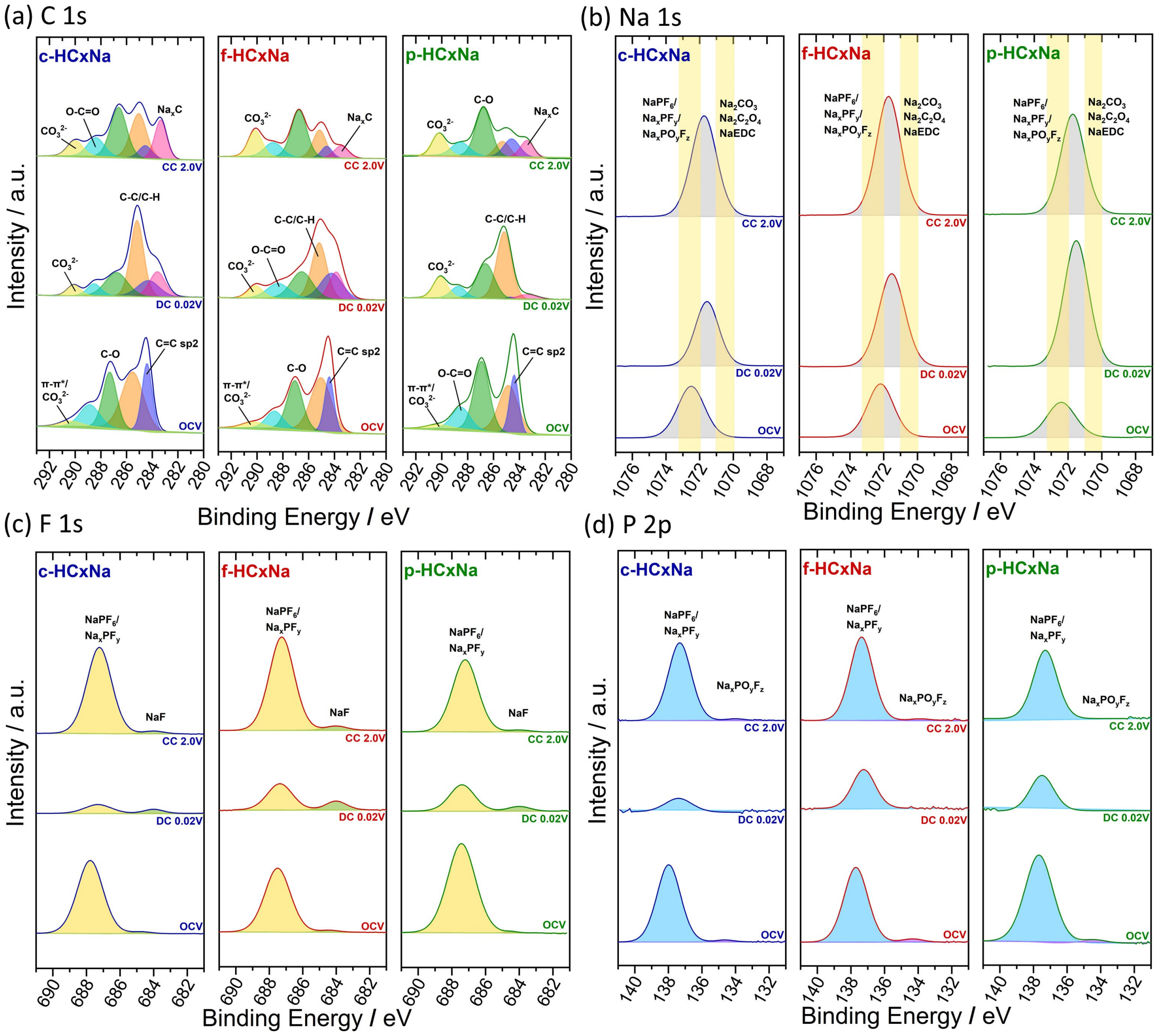

Figure 7. Photoelectron lines of the a) C 1s, b) Na 1s d) F 1s, and d) P 2p regions for c-HC, f-HC, and p-HC electrodes at OCV, fully sodiated (at 0.02 V) and de-sodiated (at 2.0 V) state of charge. The spectra have been acquired without sputtering.

(partially from CMC binder) and O–C=O species indicating the formation of the SEI covering the electrode surface. The pseudo-graphitic network peak is still observed at 0.02 V for c-HC and f-HC, but it is hardly observable for p-HC. Additionally, at lower binding energies (~283.5 eV) a peak corresponding to the sodiated HC developed,[59] which is more pronounced from c-HC and f-HC than for p-HC. Therefore, it can be assumed that the SEI formed on c-HC and f-HC electrodes are highly inhomogeneous and/or very thin, i.e., not fully protecting their surface, while the SEI for the p-HC electrode is thicker and/or more homogeneously distributed, i.e., more protective. Nonetheless, the SEI of all HCs is composed of hydrocarbons (C–C/C–H), C–O containing species, alkyl carbonates (O–C=O), and carbonates (CO_3^{2-}).

As expected,[60,61] the SEI on all HCs is not stable after the first de-sodiation (2.0 V), which explains the low CE values during the first cycles (see Figure 6a). In fact, in the de-sodiated state, the C–O, sodiated HC, O–C=O, and CO_3^{2-} contributions increase, while the hydrocarbon (C–C/C–H) decreases, indicating a thinning of the SEI due to its partial dissolution or mechanical cracking/detaching. However, the chemical composition of the SEI in all de-sodiated HCs is rather similar to that in the sodiated-state.

Figure 7b summarized the Na 1s photoelectron spectra of all HCs at different SOC. The Na 1s is a high binding energy photoelectron line and it has a very low kinetic energy and a very short inelastic mean free path, resulting in an excellent probe to elucidate the outermost region of the SEI.[62] The peak intensity/area increases upon electrochemical cycling, suggesting the formation of Na-rich species in the outermost SEI. The SEI on p-HC is richer in Na-species, most likely yielding to the high thickness already observed in the C 1s spectrum. Additionally, the peak shifts towards higher binding energies in the de-sodiated state compared to the sodiated state indicate that more fluorine-based species are formed (also confirmed by the F 1s photoelectron line in Figure 7c), while carbon-based species are the main contribution of the outermost region at de-sodiated state.

The F 1s and P 2p photoelectron lines illustrated in Figure 7c and d provide the chemistry of the products resulting from the decomposition of $NaPF_6$. For the electrode hold at OCV, two peaks are observed at 687.5 eV (F 1s) and at 137.7 eV (P 2p) corresponding to $NaPF_6$.[63,64] The contribution of Na_xPF_y, i.e., a decomposition product of the salt, obviously appears at similar binding energies of $NaPF_6$.[65,66] Therefore, the spontaneous decomposition of the salt cannot be excluded. In the F 1s and P 2p spectra of sodiated HCs, the intensity of the peak corresponding to the "pure" salt is seen to decrease, indicating that the salt is partly decomposed and incorporated in the SEI. Additionally, two peaks are observed at lower binding energies, i.e., 684.5 eV in the F 1s and 133.5 eV in the P 2p region corresponding to NaF and $Na_xPO_yF_z$, respectively, indicating the reductive decomposition of $NaPF_6$.[65]

In the de-sodiated state (2.0 V), the contribution of $NaPF_6$/Na_xPF_y is much more pronounced than that of the reduced species (NaF and $Na_xPO_yF_z$), which is in agreement with the trend observed in the C 1s region and indicates the thinning of the SEI upon de-sodiation. Additionally, as shown in the Na 1s region (see Figure 7b), the amount of F-rich species is more prominent in the de-sodiated HCs.

Overall, the surface chemistry and reactivity of the HCs upon sodiation are rather comparable. However, the SEI of p-HC is more homogeneous and/or thicker than those formed on the other HCs. However, based on the ICE values reported in Table 2, c-HC and p-HC are expected to have similar SEI thickness. Hence, the SEI on p-HC is probably more homogeneously distributed on the surface rather than thicker than that on c-HC and f-HC, which is confirmed by the disappearance of pseudo-graphitic-like peak (C=C) and the trace of sodiated HC peak in C 1s spectrum of p-HC.

In order to investigate the HCs' electrochemical behavior upon Li uptake and release, their surface chemistry was also studied by XPS. The corresponding C 1s, O 1s, F 1s, and P 2p regions of the spectra are illustrated in Figure 8.

From the peak evolution in the C 1s region (Figure 8a), a surface layer appears to be formed already on the electrodes hold at OCV, as it occurs in Na electrolyte too. In fact, the intensity of the C–C/C–H and oxidized species peaks increases with respect to the pristine electrodes. In the lithiated state (0.02 V), the SEI layer is thicker, as suggested by the disappearance of the peak corresponding to the pseudo-graphitic network of HC (C=C at 284.4 eV). Additionally, f-HC and p-HC show a thicker/more homogenous SEI layer compared to c-HC as indicated by the intensity ratio between the hydrocarbon and lithiated HC peaks. This is in accordance with the more pronounced peak at 0.5 V in the CV curves. On the other hand, the SEI on f-HC is slightly richer in C–O species, as also shown by the O 1s spectrum (Figure 8b). In contrast, the SEI on c-HC and p-HC is richer in inorganic species from $LiPF_6$ decomposition, i.e., LiF and $Li_xPO_yF_z$, as revealed by the F 1s at 685 eV and P 2p at 135.5 eV in Figure 8c and 8d, respectively. In delithiated state (2.0 V), all HCs show the pseudo-graphitic-like peak at 284.4 eV, which can be attributed to the SEI thinning due to a partial dissolution and/or cracking. This also explains the lower CE values in the initial galvanostatic cycles when compared to the sodiated electrodes (see Figure 6b). Nonetheless, for f-HC, the pseudo-graphitic-like peak is only slightly detected, suggesting that the SEI of f-HC is thicker than in c-HC and p-HC. Finally, with the exception of f-HC, the $LiPF_6$/Li_xPF_y peaks in the F 1s and P 2p regions are more pronounced than those of the reduced species (LiF and $Li_xPO_yF_z$), as it occurs in sodiated HCs, again suggesting for the instability of the SEI.

By comparing the spontaneous SEI growing on the various HC electrodes at OCV in both the Na- and Li-based electrolytes, main differences are observed in the F 1s and P 2p regions. Regarding the Na-based electrolyte, the possible spontaneous decomposition of $NaPF_6$ by chemical reactivity with the electrode is not observed. Indeed, NaF and $Na_xPO_yF_z$, which are the expected $NaPF_6$ decomposition products are not observed at OCV possibly due to their solubility in the electrolyte.[61,67] On the other hand, $LiPF_6$ salt is reduced to LiF (at 685 eV in F 1s) and $Li_xPO_yF_z$ (at 135.5 eV in P 2p), which are poorly soluble in the electrolyte. Beside the presence of the salt-related components, the surface chemistry of the HCs hold at OCV in

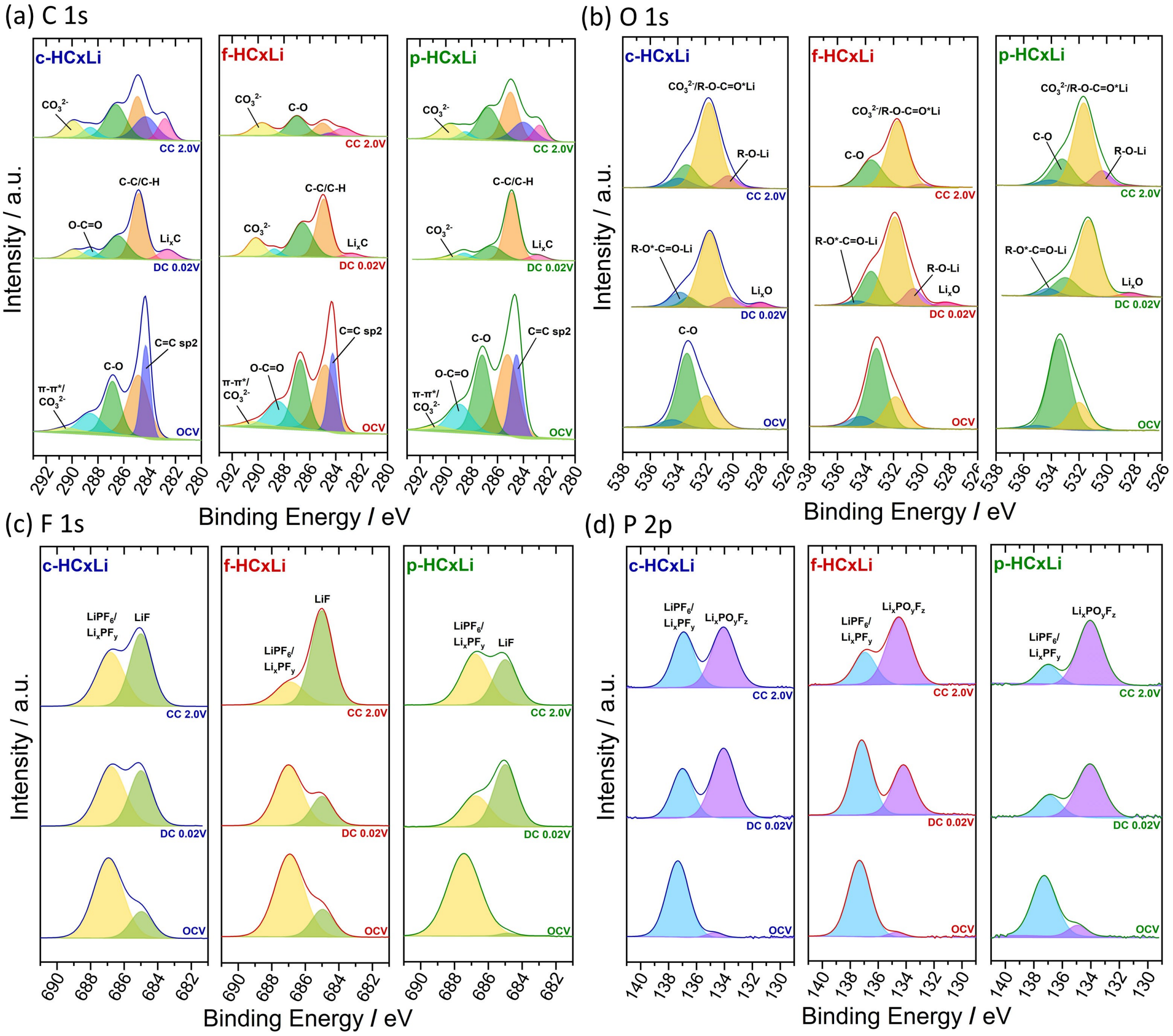

Figure 8. Photoelectron lines of the a) C 1s, b) O 1s c) F 1s, and d) P 2p regions for c-HC, f-HC, and p-HC electrodes at OCV, fully lithiated (at 0.02 V) and de-lithiated (at 2.0 V) state of charge. The spectra have been acquired without sputtering.

the Li electrolyte is comparable with that observed in the Na electrolyte.

Considering the SEI formed on the various HCs in the intercalated state (0.02 V), the chemical composition upon lithiation and sodiation is, once more, similar. Despite the carbon-based SEI species are rather similar in both systems as the main contribution is from C–C/C–H, C–O, alkyl-, and carbonates, the O 1s, F 1s, and P 2p spectra show the formation of more Li containing inorganic species, such as Li_xO at 528 eV in O1s (as well as organic R–O–Li at 530 eV),[55,68] LiF at 685 eV and $LiPF_6/Li_xPF_y$ at 687.0 eV in F 1s, and $Li_xPO_yF_z$ at 134 eV on P 2p than the corresponding Na-based compounds.[68] This suggests that upon lithiation a higher amount of inorganic compounds is formed than upon sodiation. However, the solubility of the Na-based inorganic SEI components, cannot be disregarded. The distribution of the inorganic/organic SEI species is particularly interesting, because of the opposite tendency observed in this work compared to a previous study on HC synthesized from sucrose.[55] This confirms that the precursor and the synthesis conditions strongly affect the HC microstructural properties, in turn affecting its reactivity with the electrolyte and thus the chemical composition of the SEI. However, since a different electrolyte was used in the previously reported study, i.e., 1 M $NaClO_4$ in PC, it is worth noting that the influence of the electrolyte cannot be excluded.

Finally, at the de-sodiated/de-lithiated state (2.0 V), similar chemical differences are observed in the SEI grown on sodiated and lithiated HC electrodes. Lithiated electrodes show more pronounced presence of salt decomposition products (LiF at 685 eV in F 1s and $Li_xPO_yF_z$ at 137 eV in P 2p), might be due to the less soluble Li-based inorganic species compared to Na ones. Most likely, the different solubilities of the Na- and Li-salts might be one of the reasons for the formation of a thicker SEI on Li-based electrodes than Na ones. It is worth noting that the pseudo-graphitic-like peak disappeared in the lithiated HCs, while it was still observed in the sodiated ones (see Figures 8a and 7a, respectively), in agreement with the lower ICE values observed upon lithiation compared to sodiation (see Table 2).

To get insights into chemical composition throughout the SEI, XPS spectra were acquired at different sputtering depth of

HC electrodes extracted from Na- (Figure 9a–c at 0.02 V and 9d-f at 2.0 V) and Li cells (Figure 9g–i at 0.02 V and 9j-l at 2.0 V).

The in-depth SEI composition for the sodiated/lithiated states shows a few similarities. The amount of C–C/C–H, C–O, Na–/Li–PF$_6$ decreases getting deeper into the SEI, while the sodiated/lithiated carbon (Na$_x$C/Li$_x$C) signal, coming from the electrode bulk, increases upon sputtering due to the SEI removal by ion bombardment. The concentration of Na–/Li–F and Na$_x$-/Li$_x$–PO$_y$F$_z$ increases at higher depth, indicating that the salt is preferentially reduced near the electrode surface. However, the carbonate species exhibit different trends for the sodiated and lithiated HC electrodes. The carbonate content

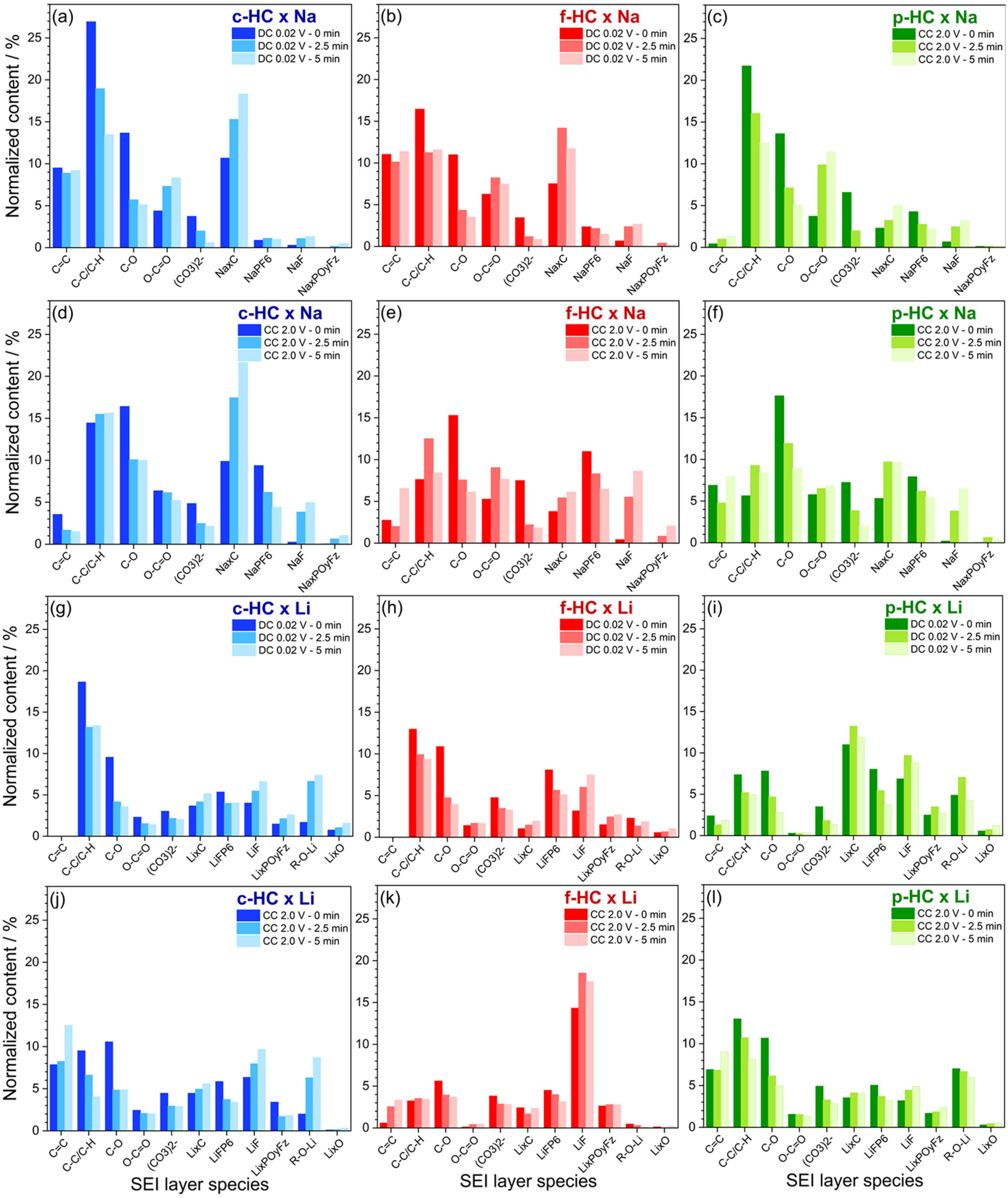

Figure 9. Normalized concentration of SEI species at different sputtering time (0, 2.5, and 5 min) of the three HCs at fully sodiated/lithiated (0.02 V) and at de-sodiated/-lithiated (2.0 V) states of charge in Na and Li cells. Na cells at 0.02 V: a) c-HC, b) f-HC, and c) p-HC; at 2.0 V: d) c-HC, e) f-HC, and f) p-HC. Li cells at 0.02 V: g) c-HC, h) f-HC, and i) p-HC; at 2.0 V: j) c-HC, k) f-HC, and l) p-HC.

drops upon sputtering of the Na–SEI, but only slight changes in the Li–SEI. On the other hand, the amount of alkyl carbonates (O–C=O) increases upon sputtering of the SEI grown upon sodiation, but shows a more stable contribution of these species throughout the whole SEI grown upon lithiation. Interestingly, the variation of the chemical composition is similar for all HC electrodes, suggesting that the surface chemistry of the HCs does not strongly affect the electrolyte decomposition products and that the SEI properties are more affected by the electrolyte components. On the other hand, the SEI on the HCs at de-sodiated/de-lithiated state show a significant decrease in the C–C/C–H content with respect to the sodiated/lithiated state. In the sodiated electrodes, however, the C–C/C–H content increases at higher depths whereas it decreases in the lithiated electrodes. The C–O, carbonates, and Na–/Li–PF_6 species decrease at higher depth in both the Na–SEI and Li–SEI of sodiated/lithiated HC electrodes as the corresponding species are more observed in the outermost region. Meanwhile, the concentration of the alkyl-carbonate and sodiated/lithiated HC is constant at all depths, which can be the result of an incomplete de-insertion of the charge carriers. The concentration of the species increases only slightly as the SEI is removed. Finally, the concentration of salt reduction products (Na–/Li–F and Na_x–/Li_x–PO_yF_z) increases close to the electrode surface, as the reduction process occurs upon sodiation/lithiation.

In summary, the chemical composition of the SEI formed on HC electrodes upon sodiation and lithiation does not depend on the active material, being very similar for all HC electrodes. However, the properties of the SEI are different. For instance, the SEI of p-HC upon sodiation is more homogeneous than those of c-HC and f-HC. On the other hand, a thicker Li–SEI is formed on f-HC and p-HC than on c-HC. Furthermore, the main difference between the SEI grown in Na- and Li cells is the higher thickness due to the higher $LiPF_6$ reactivity resulting in the formation of insoluble inorganic species (LiF and $Li_xPO_yF_z$).

3. Conclusions

In this study, three HC materials have been obtained by using different precursors and treating conditions targeting at obtaining different structural properties. The influence of the different structures, microstructures, and morphologies on the electrochemical performance and the stability of SEI has been investigated and associated with the surface reactivity, cycling stability, and rate performance. The electrochemical behavior of the various HCs upon sodiation and lithiation has been evaluated from a bulk and surface perspective enabling a structure-function correlation identification. The results indicate that the different behavior of the HCs upon sodiation and lithiation can be attributed to the surface reactivity of the HCs with the electrolyte (SEI formation and its stability), and to the structural properties of the three HCs offering storage sites preferentially reacting with Na^+ or Li^+ ions.

Overall, the following main conclusions can be derived for the three different HCs investigated in this work:

i. The HC anode derived from sustainable lignin-based bio-waste outperforms the other investigated materials with respect to both Na- and Li-storage, suggesting that beside the different synthesis conditions the choice of the precursor strongly affects the electrochemical properties.
ii. Na-storage in any HCs outperforms Li-storage in terms of capacity retention, coulombic efficiency and rate performance.
iii. It is found that the defect concentration and surface functionalities strongly affect the sloping capacity for Na-storage, while the degree of order (even though the existence of limit is also found), surface graphene layer, and the ultramicroporosity are highly related to the plateau capacity. Meanwhile, the lithiation is affected to a larger extent by the in-plane defect concentration and porosity, however, a slower kinetics is required to achieve the plateau capacity in Li-storage. The porosity in general strongly influences the CE values for both systems, with Li system reporting always less favorable values. This is directly associated with the formation and stability of the SEI.
iv. The capacity exhibited in the low potential plateau region is affected by the processes occurring in the sloping potential region, suggesting an interconnection between sloping and plateau capacity in both systems. Indeed, while from one side, a larger amount of defects induces a higher capacity in the sloping region, on the other side, they could also kinetically hinder subsequent Na^+ ion storage in the TLPG-NDs and ultramicropores structures. Meanwhile, structures with fewer defect sites in the TLPG-ND facilitate the transfer and insertion of ions into the domain and ultramicropores.
v. The chemical composition of the SEI formed upon sodiation and lithiation does not strongly depend on the HC surface properties, but rather on the chemical/electrochemical stability of the electrolyte and its decomposition products as suggested by the similar decomposition products observed within Li and Na cells employing the three different HC electrodes.
vi. The SEI formed upon lithiation is thicker, suggesting for an increased reactivity of the Li salts. The thinner SEI formed upon sodiation could, however, also be attributed to increased solubility of the Na-salt decomposition products and instability of the SEI (breathing effect).
vii. The slightly different properties of the SEI in relation to the three different HC in Li and Na systems can be associated with the different SSA and open porosity, as indicated by the CE values in both systems.

This study highlights again that besides the similar chemistry of Li and Na, a direct knowledge transfer from the Li-based technology to SIB is not straightforward, suggesting that an optimized HC for Li^+ ions storage might not be the optimal system for Na^+ ions storage and vice versa. For instance, the porous structure and size play a key role in the electrochemistry of HCs. Indeed, depending on their shape, size, and pores could appear as open or closed to Li^+ or Na^+ ions thus differentiating their storage mechanism. Beside the lack of a universally accepted structure-function correlation, it is clear that wheater the obtainment of high-performance anode will arise from a fundamental understanding of the HC's structure or from technological improvements (i.e. materials process optimization) is still an open question. While industries will have an impact on the latter one, the research community efforts should be devoted to further operando studies which are seen as the key to unveil the dilemma behind the structure/function correlation in HC anodes.

Acknowledgments

H.M., M.Z., I.H., and S.P. acknowledge support from the project TRANSITION (03XP0186) funded by the Bundesministerium für Bildung und Forschung (BMBF) and the basic funding from the Helmholtz Gemeinschaft. KISCO Deutschland GmbH is kindly acknowledged for providing BELLFINE® LN0001 hard carbon (AT ELETRODE.CO.,LTD). Open access funding enabled and organized by Projekt DEAL.

Conflict of Interest

The authors declare no conflict of interest.

Keywords: sodium-ion batteries · hard carbon · anode · solid electrolyte interphase · microstructure

[1] C. Vaalma, D. Buchholz, M. Weil, S. Passerini, *Nat. Rev. Mater.* **2018**, *3*.
[2] E. de la Llave, V. Borgel, K.-J. J. Park, J.-Y. Y. Hwang, Y.-K. K. Sun, P. Hartmann, F. F. Chesneau, D. Aurbach, *ACS Appl. Mater. Interfaces* **2015**, *8*, 1867–1875.
[3] A. Kamiyama, K. Kubota, T. Nakano, S. Fujimura, S. Shiraishi, H. Tsukada, S. Komaba, *ACS Appl. Mater. Interfaces* **2020**, *3*, 135–140.
[4] I. Hasa, S. Mariyappan, D. Saurel, P. Adelhelm, A. Y. Koposov, C. Masquelier, L. Croguennec, M. Casas-Cabanas, *J. Power Sources* **2021**, *482*, 228872.
[5] https://news.cnrs.fr/articles/a-battery-revolution-in-motion.
[6] https://www.faradion.co.uk/.
[7] https://www.hinabattery.com/en/.
[8] https://natron.energy/.
[9] A. Bauer, J. Song, S. Vail, W. Pan, J. Barker, Y. Lu, *Adv. Energy Mater.* **2018**, *8*, 1702869.
[10] A. Yoshino, *Angew. Chem. Int. Ed.* **2012**, *51*, 5798–5800.
[11] M. Li, J. Lu, Z. Chen, K. Amine, *Adv. Mater.* **2018**, *30*, 1800561.
[12] D. A. Stevens, J. R. Dahn, *J. Electrochem. Soc.* **2001**, *148*, A803–A811.
[13] R. Alcántara, J. M. Jiménez Mateos, J. L. Tirado, *J. Electrochem. Soc.* **2002**, *149*, A201.
[14] X. Xia, M. N. Obrovac, J. R. Dahn, *Electrochem. Solid-State Lett.* **2011**, *14*, A130.
[15] H. Y. Yu, H. J. Liang, Z. Y. Gu, Y. F. Meng, M. Yang, M. X. Yu, C. De Zhao, X. L. Wu, *Electrochim. Acta* **2020**, *361*, 137041.
[16] W. Lv, F. Wen, J. Xiang, J. Zhao, L. Li, L. Wang, Z. Liu, Y. Tian, *Electrochim. Acta* **2015**, *176*, 533–541.
[17] X. Dou, I. Hasa, D. Saurel, C. Vaalma, L. Wu, D. Buchholz, D. Bresser, S. Komaba, S. Passerini, *Mater. Today* **2019**, *23*, 87–104.
[18] M. Á. Muñoz-Márquez, D. Saurel, J. L. Gómez-Cámer, M. Casas-Cabanas, E. Castillo-Martínez, T. Rojo, *Adv. Energy Mater.* **2017**, *7*, 1700463.
[19] D. A. Stevens, J. R. Dahn, *J. Electrochem. Soc.* **2000**, *147*, 4428–4431.
[20] J. M. Stratford, P. K. Allan, O. Pecher, P. A. Chater, C. P. Grey, *Chem. Commun.* **2016**, *52*, 12430–12433.
[21] J. S. Weaving, A. Lim, J. Millichamp, T. P. Neville, D. Ledwoch, E. Kendrick, P. F. Mcmillan, P. R. Shearing, C. A. Howard, D. J. L. Brett, *ACS Appl. Mater. Interfaces* **2020**, *3*, 7474–7484.
[22] B. Zhang, C. M. Ghimbeu, C. Laberty, C. Vix-Guterl, J. M. Tarascon, *Adv. Energy Mater.* **2016**, *6*, 1501588.
[23] C. Bommier, T. W. Surta, M. Dolgos, X. Ji, *Nano Lett.* **2015**, *15*, 5888–5892.
[24] M. Anji Reddy, M. Helen, A. Groß, M. Fichtner, H. Euchner, *ACS Energy Lett.* **2018**, *3*, 2851–2857.
[25] S. Alvin, D. Yoon, C. Chandra, H. S. Cahyadi, J. H. Park, W. Chang, K. Y. Chung, J. Kim, *Carbon* **2019**, *145*, 67–81.
[26] Y. Morikawa, S. Nishimura, R. Hashimoto, M. Ohnuma, A. Yamada, *Adv. Energy Mater.* **2020**, *10*, 1903176.
[27] M. A. Reddy, M. Helen, A. Groß, M. Fichtner, H. Euchner, *ACS Energy Lett.* **2018**, *3*, 2851–2857.
[28] Z. Li, C. Bommier, Z. Sen Chong, Z. Jian, T. W. Surta, X. Wang, Z. Xing, J. C. Neuefeind, W. F. Stickle, M. Dolgos, P. A. Greaney, X. Ji, *Adv. Energy Mater.* **2017**, *7*, 1602894.
[29] P. Thomas, D. Billaud, *Electrochim. Acta* **2002**, *47*, 3303–3307.
[30] C. Zhao, Q. Wang, Y. Lu, B. Li, L. Chen, Y. S. Hu, *Sci. Bull.* **2018**, *63*, 1125–1129.
[31] D. Saurel, B. Orayech, B. Xiao, D. Carriazo, X. Li, T. Rojo, *Adv. Energy Mater.* **2018**, *8*, 1703268.
[32] X. Dou, I. Hasa, M. Hekmatfar, T. Diemant, R. J. Behm, D. Buchholz, S. Passerini, *ChemSusChem* **2017**, *10*, 2668–2676.
[33] X. Dou, I. Hasa, D. Saurel, M. Jauregui, D. Buchholz, T. Rojo, S. Passerini, *ChemSusChem* **2018**, *11*, 3276–3285.
[34] K. L. Hong, L. Qie, R. Zeng, Z. Q. Yi, W. Zhang, D. Wang, W. Yin, C. Wu, Q. J. Fan, W. X. Zhang, Y. H. Huang, *J. Mater. Chem. A* **2014**, *2*, 12733–12738.
[35] A. C. J. Walton, P. Wincott, N. Fairley, *Peak Fitting with CasaXPS: A Casa Pocket Book*, Accolyte Science, Knutsford, **2010**.
[36] C. D. Wagner, W. M. Riggs, L. E. Davis, J. F. Moulder, G. E. Mullenberg, *Handbook of X-Ray Photoelectron Spectroscopy*, Perkin-Elmer Corporation, **1979**.
[37] T. Ohzuku, Y. Iwakoshi, K. Sawai, *J. Electrochem. Soc.* **1993**, *140*, 2490–2498.
[38] W. Xing, J. R. Dahn, *J. Electrochem. Soc.* **1997**, *144*, 1195–1201.
[39] A. Sadezky, H. Muckenhuber, H. Grothe, R. Niessner, U. Pöschl, *Carbon* **2005**, *43*, 1731–1742.
[40] A. C. Ferrari, J. Robertson, *Phys. Rev. B* **2000**, *61*, 14095–14107.
[41] A. Eckmann, A. Felten, A. Mishchenko, L. Britnell, R. Krupke, K. S. Novoselov, C. Casiraghi, *Nano Lett.* **2012**, *12*, 3925–3930.
[42] D. Saurel, J. Segalini, M. Jauregui, A. Pendashteh, B. Daffos, P. Simon, M. Casas-Cabanas, *Energy Storage Mater.* **2019**, *21*, 162–173.
[43] W. Ruland, *Adv. Mater.* **1990**, *2*, 528–536.
[44] P. Adelhelm, Novel Carbon Materials with Hierarchical Porosity: Templating Strategies and Advanced Characterization, **2007** https://publishup.uni-potsdam.de/opus4-ubp/frontdoor/index/index/year/2007/docId/1387.
[45] J. R. Dahn, W. Xing, Y. Gao, *Carbon* **1997**, *35*, 825–830.
[46] D. Larcher, C. Mudalige, M. Gharghouri, J. R. Dahn, *Electrochim. Acta* **1999**, *44*, 4069–4072.
[47] M. B. Vázquez-Santos, E. Geissler, K. László, J. N. Rouzaud, A. Martínez-Alonso, J. M. D. Tascón, *J. Phys. Chem. C* **2012**, *116*, 257–268.
[48] C. Matei Ghimbeu, J. Górka, V. Simone, L. Simonin, S. Martinet, C. Vix-Guterl, *Nano Energy* **2018**, *44*, 327–335.
[49] M. Thommes, K. A. Cychosz, *Adsorption* **2014**, *20*, 233–250.
[50] M. Thommes, K. Kaneko, A. V. Neimark, J. P. Olivier, F. Rodriguez-Reinoso, J. Rouquerol, K. S. W. Sing, *Pure Appl. Chem.* **2015**, *87*, 1051–1069.
[51] H. Kumar, E. Detsi, D. P. Abraham, V. B. Shenoy, *Chem. Mater.* **2016**, *28*, 8930–8941.
[52] S. Alvin, H. S. Cahyadi, J. Hwang, W. Chang, S. K. Kwak, J. Kim, *Adv. Energy Mater.* **2020**, *10*, 2000283.
[53] S. Qiu, L. Xiao, M. L. Sushko, K. S. Han, Y. Shao, M. Yan, X. Liang, L. Mai, J. Feng, Y. Cao, X. Ai, H. Yang, J. Liu, *Adv. Energy Mater.* **2017**, *7*, 1700403.
[54] R. I. R. Blyth, H. Buqa, F. P. Netzer, M. G. Ramsey, J. O. Besenhard, P. Golob, M. Winter, *Appl. Surf. Sci.* **2000**, *167*, 99–106.
[55] S. Komaba, W. Murata, T. Ishikawa, N. Yabuuchi, T. Ozeki, T. Nakayama, A. Ogata, K. Gotoh, K. Fujiwara, *Adv. Funct. Mater.* **2011**, *21*, 3859–3867.
[56] S. Doubaji, B. Philippe, I. Saadoune, M. Gorgoi, T. Gustafsson, A. Solhy, M. Valvo, K. Edström, *ChemSusChem* **2016**, *9*, 97–108.

[57] M. A. Muñoz-Márquez, M. Zarrabeitia, E. Castillo-Martínez, A. Eguía-Barrio, T. Rojo, M. Casas-Cabanas, *ACS Appl. Mater. Interfaces* **2015**, *7*, 7801–7808.
[58] M. Zarrabeitia, L. Gomes Chagas, M. Kuenzel, E. Gonzalo, T. Rojo, S. Passerini, M. Á. Muñoz-Márquez, *ACS Appl. Mater. Interfaces* **2019**, *11*, 28885–28893.
[59] A. Ponrouch, R. Dedryvère, D. Monti, A. E. Demet, J. M. Ateba Mba, L. Croguennec, C. Masquelier, P. Johansson, M. R. Palacín, *Energy Environ. Sci.* **2013**, *6*, 2361.
[60] J. Song, B. Xiao, Y. Lin, K. Xu, X. Li, *Adv. Energy Mater.* **2018**, *8*, 1703082.
[61] R. Mogensen, D. Brandell, R. Younesi, *ACS Energy Lett.* **2016**, *1*, 1173–1178.
[62] H. Shinotsuka, S. Tanuma, C. J. Powell, D. R. Penn, *Surf. Interface Anal.* **2015**, *47*, 871–888.
[63] J. Fondard, E. Irisarri, C. Courrèges, M. R. Palacin, A. Ponrouch, R. Dedryvère, *J. Electrochem. Soc.* **2020**, *167*, 070526.
[64] Y. Pan, Y. Zhang, B. S. Parimalam, C. C. Nguyen, G. Wang, B. L. Lucht, *J. Electroanal. Chem.* **2017**, *799*, 181–186.
[65] M. Dahbi, T. Nakano, N. Yabuuchi, S. Fujimura, K. Chihara, K. Kubota, J. Y. Son, Y. T. Cui, H. Oji, S. Komaba, *ChemElectroChem* **2016**, *3*, 1856–1867.
[66] C. Krishnaraj, A. M. Kaczmarek, H. S. Jena, K. Leus, N. Chaoui, J. Schmidt, R. Van Deun, P. Van Der Voort, *ACS Appl. Mater. Interfaces* **2019**, *11*, 27343–27352.
[67] G. G. Eshetu, T. Diemant, M. Hekmatfar, S. Grugeon, R. J. Behm, S. Laruelle, M. Armand, S. Passerini, *Nano Energy* **2019**, *55*, 327–340.
[68] S. Malmgren, K. Ciosek, R. Lindblad, S. Plogmaker, J. Kühn, H. Rensmo, K. Edström, M. Hahlin, *Electrochim. Acta* **2013**, *105*, 83–91.

Manuscript received: December 15, 2020
Revised manuscript received: February 28, 2021
Accepted manuscript online: March 1, 2021
Version of record online: March 15, 2021